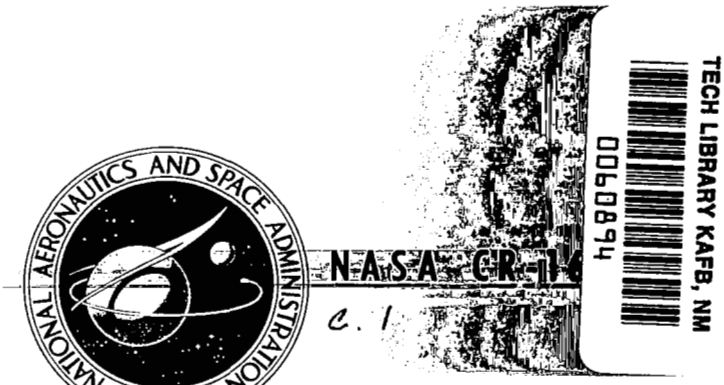

NASA CONTRACTOR REPORT

NASA CR-1659

ADVANCED FIGURE SENSOR

by Robert Crane, Jr.

Prepared by
PERKIN-ELMER CORPORATION
Norwalk, Conn.
for Electronics Research Center

NATIONAL AERONAUTICS AND SPACE ADMINISTRATION • WASHINGTON, D. C. • SEPTEMBER 1970

1. Report No.	2. Government Accession No.	3. Recipient's Catalog No.
NASA CR-1659		
4. Title and Subtitle		**5. Report Date**
ADVANCED FIGURE SENSOR		September 1970
		6. Performing Organization Code
7. Author(s)		**8. Performing Organization Report No.**
Robert Crane, Jr.		
9. Performing Organization Name and Address		**10. Work Unit No.**
The Perkin-Elmer Corporation Norwalk, Connecticut		**11. Contract or Grant No.** NAS 12-681
		13. Type of Report and Period Covered
12. Sponsoring Agency Name and Address		Contractor Report
National Aeronautics and Space Administration Washington, D.C. 20546		**14. Sponsoring Agency Code**

15. Supplementary Notes

16. Abstract

The purpose of the Advanced Figure Sensor project was to investigate key elements in an optical figure sensor suitable for eventual use in a spaceborne active optics telescope. The specific objectives were to develop: 1) a solid state optical frequency shifter, 2) a technique for measuring a parabolic primary mirror, and 3) a concept for measuring the alignment of the secondary mirror. The basic figure sensor employs an interference phase measuring interferometer combined with electronic circuits for making measurements in real time.

17. Key Words (Selected by Author(s))	18. Distribution Statement
	Unclassified - Unlimited

19. Security Classif. (of this report)	20. Security Classif. (of this page)	21. No. of Pages	22. Price*
Unclassified	Unclassified	85	$3.00

*For sale by the Clearinghouse for Federal Scientific and Technical Information Springfield, Virginia 22151

TABLE OF CONTENTS

LIST OF ILLUSTRATIONS

LIST OF ILLUSTRATIONS (CONTINUED)

1. SUMMARY

The purpose of the Advanced Figure Sensor project was to investigate key elements in an optical figure sensor suitable for eventual use in a spaceborne active optics telescope. The specific objectives were to develop: 1) a solid state optical frequency shifter, 2) a technique for measuring a parabolic primary mirror, and 3) a concept for measuring the alignment of the secondary mirror. The basic figure sensor employs an interference phase measuring interferometer combined with electronic circuits for making measurements in real time.

Two approaches were investigated for the frequency shifter:

(1) Doppler frequency shift by mechanical translation of a reference reflector

(2) Rotating 1/4 λ plate in circularly polarized light, where rotating birefringence effect is produced by a rotating shear stress wave in an electro-acoustical-optical device.

The Doppler approach was selected because of its simplicity and ease of manufacture. The breadboard unit consisted of a reference mirror mounted in a piezoelectric cylinder. A triangular waveform electronic drive generates a cyclic displacement of 4 λ per excursion at a rate that produces an optical frequency shift of $\pm$ 500 Hz.

Three approaches were investigated for the aspheric measurement technique:

(1) An aspheric reference reflector that generates wavefront distortions identical to the optical path difference between the parabola and a reference sphere.

(2) A null corrector that generates spherical aberrations that are exactly complimentary to the spherical aberrations of a parabola when viewed from its paraxial center of curvature.

(3) Analysis of the moiré pattern resulting from the superposition of a real and a calculated fringe pattern resulting from the optical path difference between the parabola and a spherical reference reflector.

The moiré pattern approach was selected because it offered greater flexibility, and fewer optical elements that might introduce figure errors, and the calculated fringe pattern is relatively simple to manufacture. A reference pattern was designed and made to measure an 8-inch f/1 parabola. Tests showed that the technique can be used with the phase measuring interferometer with no added complexity. Tests with a good f/1, 8-inch parabola showed that the technique is practical, but more calculations must be performed to make a perfect reference pattern.

An optical arrangement was investigated for measuring the secondary alignment with the primary mirror figure sensor. Calculations indicate that tilt alignment can be measured with the required accuracy. Axial alignment must be monitored at the instrument focal plane.

A recommended optical arrangement and block diagram has been developed for a working model figure sensor that uses the Doppler frequency shifter and moiré pattern analysis.

2. INTRODUCTION

2.1 Objectives

The concept of Active Optics for large astronomical telescopes consists of measuring the optical figure of the primary mirror; computing any errors; and automatically realigning the mirror to its original design figure, either by positioning pieces of a segmented mirror or by flexing a relatively thin mirror (Refs. 1,2). (See Figure 1.) A variety of optical test devices have been evaluated for the figure sensing; however, interferometric measurements are the only ones that produce quantitative data with the required accuracy and short response time required for an automatic control system.

In the active optics application, one beam of a Twyman-Green interferometer is reflected from a plane reference reflector; the second beam is converted by a lens to a diverging spherical wavefront. (See Figure 2.) The figure sensor is located so that the diverging wavefront is concentric about the center of curvature of the mirror under test. If the mirror has a spherical surface and is aligned so that its center of curvature is located at the center of divergence of the wavefront, the light will be reflected back exactly upon its incident path. It will then pass back through the lens and again become a plane wavefront. Thus, for a perfect spherical mirror, interference takes place at the beamsplitter between two coplanar wavefronts. When there are surface irregularities on the mirror under test, or when it is misaligned, the return wavefront will not be coplanar with the reference wavefront at the point of interference. For tilt misalignment, the interference wavefronts will be approximately plane but not parallel, producing a fringe pattern consisting of straight lines. For axial misalignment, interference will take place between a plane wavefront and a slightly spherical wavefront. This produces a circular fringe pattern. Small localized figure errors produce localized phase shifts in the fringe pattern.

In a practical telescope, the primary mirror will not have a spherical figure, but will probably be close to a parabola. Therefore, techniques are required to adapt the figure sensor to aspheric mirror measurements.

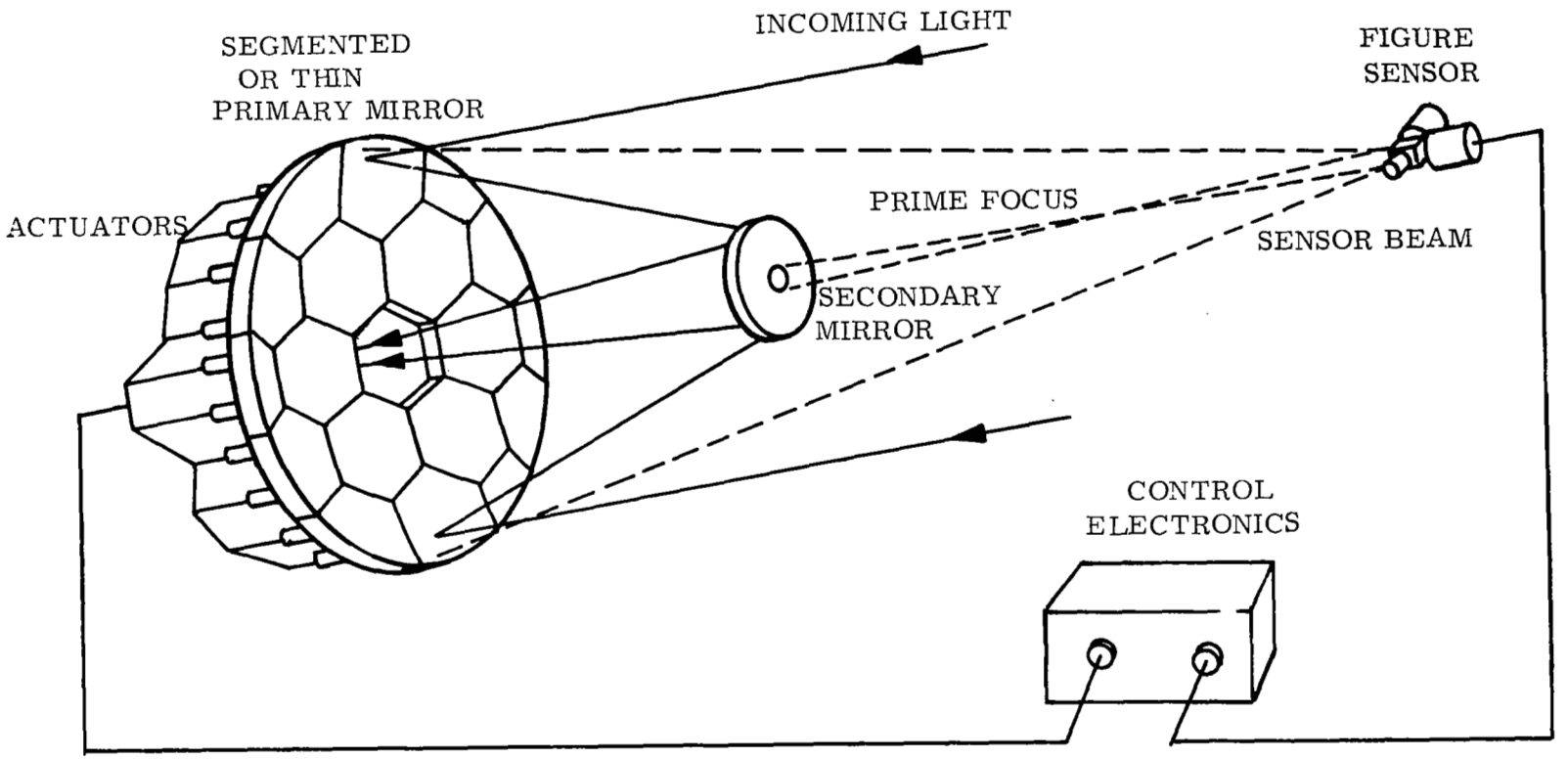

Figure 1. Active Optics Concept

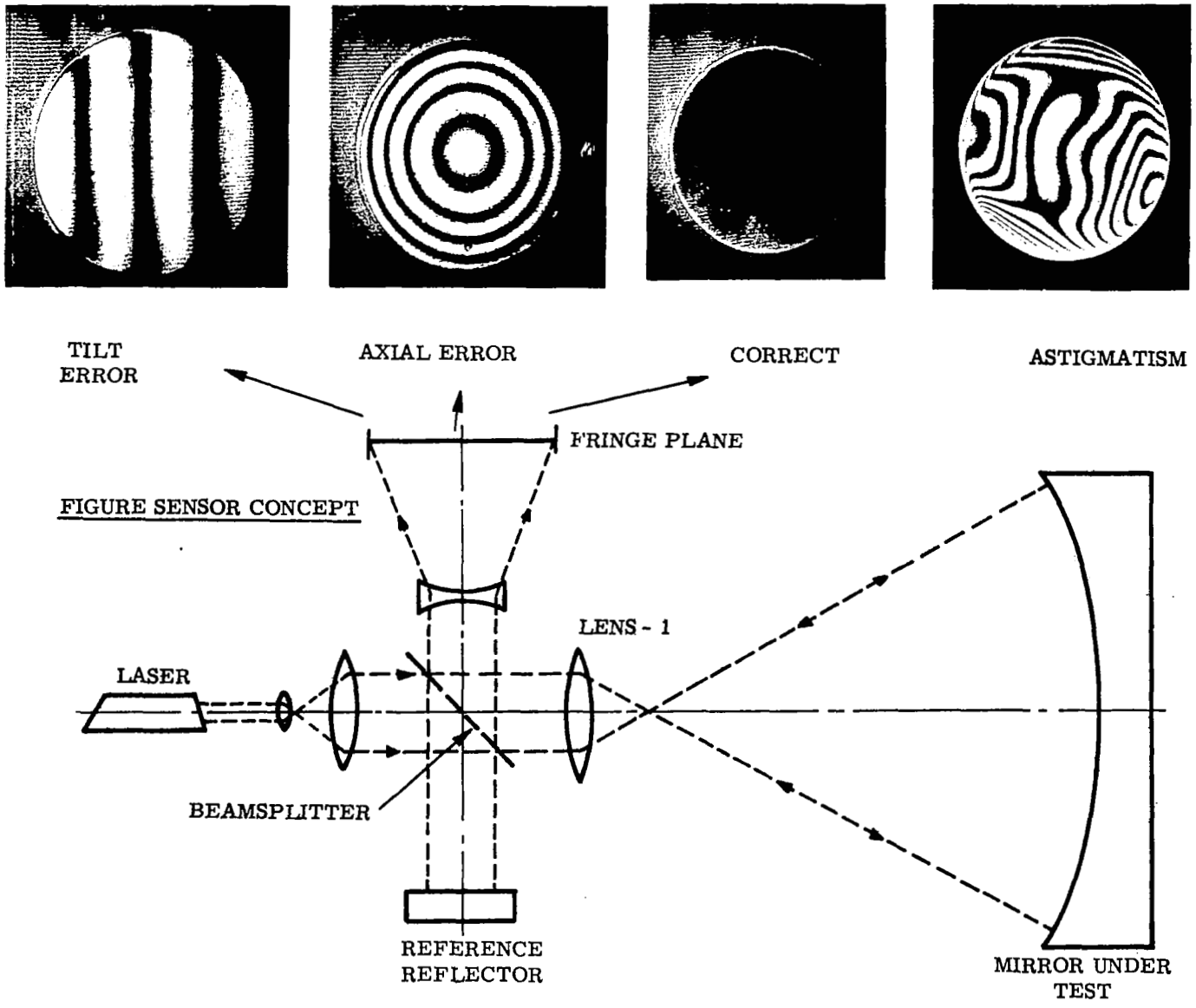

Figure 2. Figure Sensor Concept

The figure of the primary mirror in a spaceborne telescope must be maintained with an accuracy that will provide diffraction-limited performance. This means that the figure sensor must be able to detect not just interference fringes but errors that result in only small fractions of a fringe. The concept of electronic optical phase measurement was developed to provide this accuracy. This concept has been described in detail by a number of previous publications (Refs 3,4,5,6) and will be described only briefly here.

The electronic phase measuring interferometer is a two-beam interferometer in which optical wavefront phase is converted to an electronic carrier phase and is then electronically analyzed. This makes it possible to sense figure errors in real time. Figure 3 is a schematic of a simplified version of the phase measuring interferometer with coherent illumination and with plane reflecting surfaces in each interference beam. If both reflectors are perfectly plane and parallel to the wavefront, interference will occur between two plane parallel wavefronts producing a light pattern with uniform intensity over its entirety. If the reference reflector is translated at constant velocity along the optical axis normal to the wavefront, then the light pattern intensity will vary through maximum and minimum levels in a sinusoidal fashion with identical phase over the entire pattern. Two detectors are placed in the output plane: one at a position arbitrarily selected as a reference, and one at a spot corresponding to a spot of unknown figure on the test surface. These convert the cycling light pattern into two cycling electronic voltages or carriers. If a small portion of the test surface is high in relation to the rest of the surface, there will be a relative phase shift of the electronic signal generated from the corresponding point in the light pattern.

In a practical implementation of this concept, linear translation of the reference reflector is regarded as causing a continuously increasing phase shift in the reference beam. Continuous increase in phase of a carrier is the same as a fixed change in frequency. Thus, an optical <u>frequency shifter</u> is required for the electronic phase measuring interferometer.

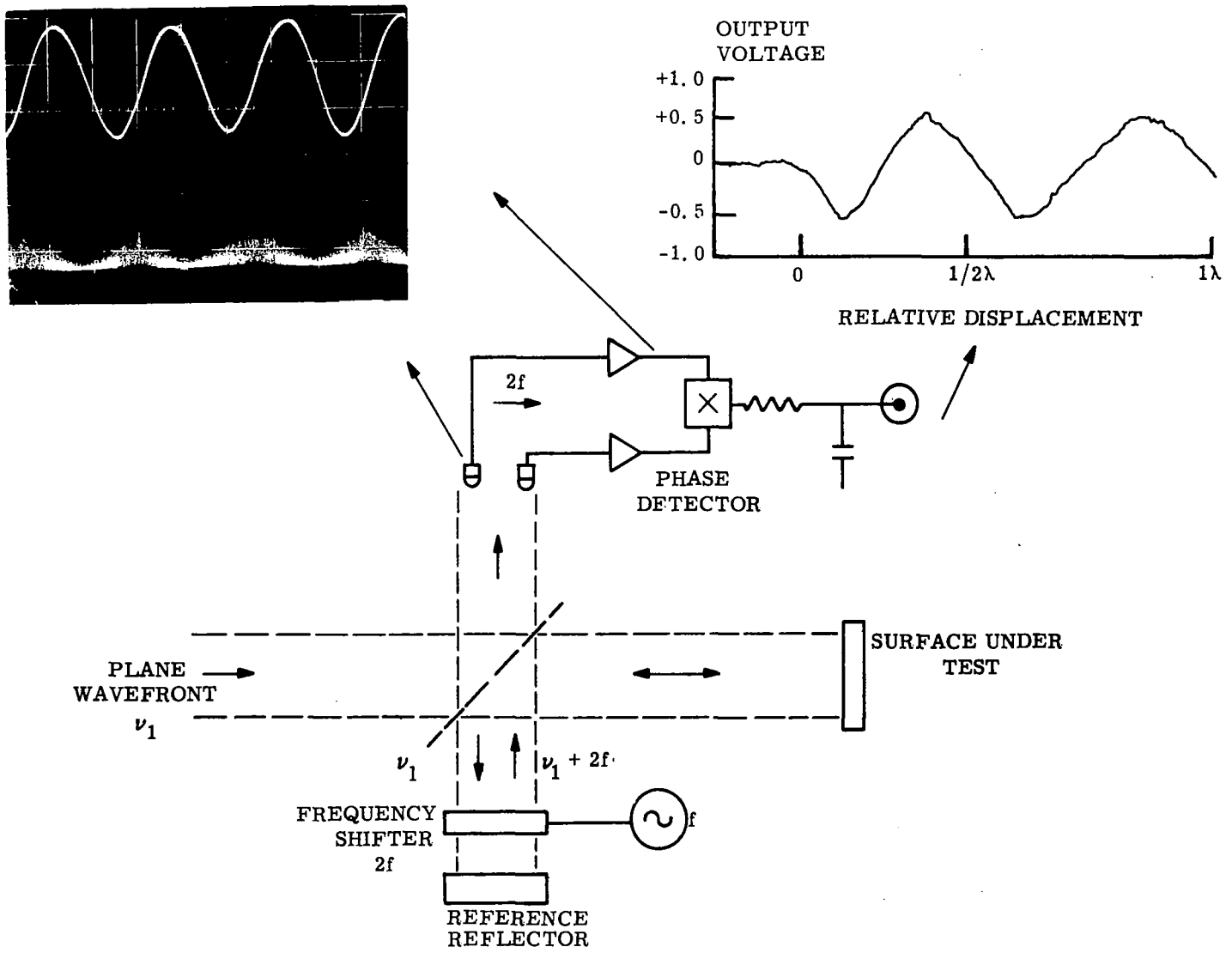

Figure 3. Phase Measuring Interferometer Concept

Therefore, the primary objectives of this project were to:

(1) Design, fabricate, test, and evaluate two different solid-state frequency shifters for use in a phase measuring interferometer.

(2) Design, fabricate, test, and evaluate the necessary optics to render the Twyman-Green interferometer capable of measuring an 8-inch-diameter, f/1 parabola.

A secondary objective was to:

(3) Study the problem of primary-to-secondary alignment in a space telescope with regard to the possibility of using the primary-mirror figure sensor to measure secondary alignment also.

2.2 Conclusions

A summary of the work completed is presented in Figures 4 through 10.

A Doppler frequency shifter was selected because it is simple and was shown to work successfully. Figure 4 shows the mechanical assembly, consisting of a reference reflector mounted in a piezoelectric cylinder. When voltage is applied between the inner and outer walls, a piezoelectric effect causes the cylinder length to change, in turn causing the reflector to translate in an axial direction. Figure 5 shows how this device is used in a Twyman-Green interferometer. A cyclic linear drive voltage is applied to the cylinder. This produces a sine wave variation of the interference light pattern, which in turn produces two sine wave carrier signals. The discontinuities in the output waveforms shown in Figure 5 occur when the drive voltage reverses direction. The frequency of the output carrier is equal to the frequency shift of the optical beam in the reference arm.

The problem involved in the measurement of an aspheric reflector, i.e., an aspheric surface is not equidistant from its nominal center of curvature, is shown in Figure 6. This figure shows the difference between a parabola and a circle of the same paraxial radius when viewed from their nominal centers of curvature. The "Δ path difference" of up to 100 wavelengths must be accommodated in the figure sensor. The selected solution uses a moiré analysis in

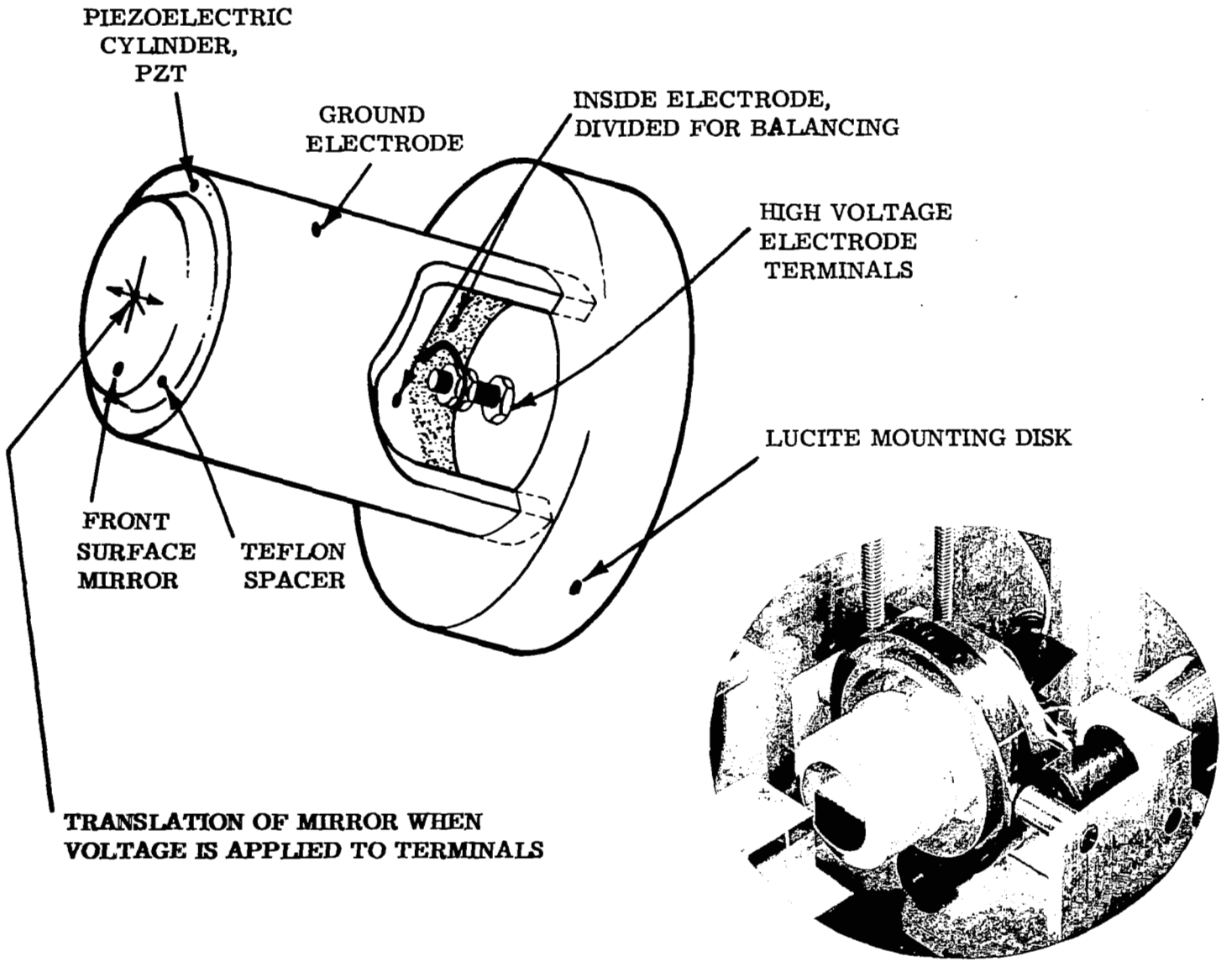

Figure 4. Frequency Shifter Assembly

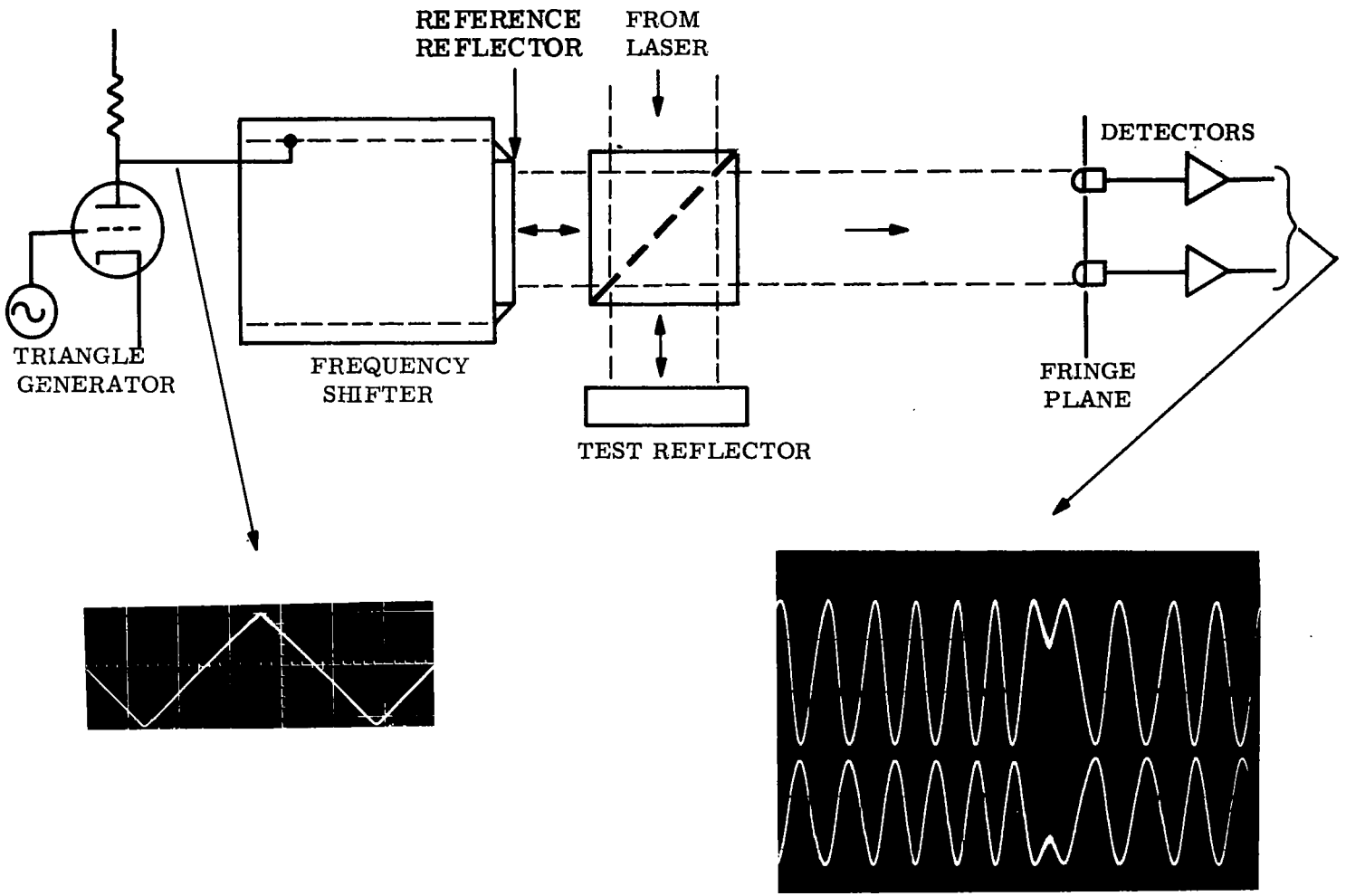

Figure 5. Frequency Shifter Operation

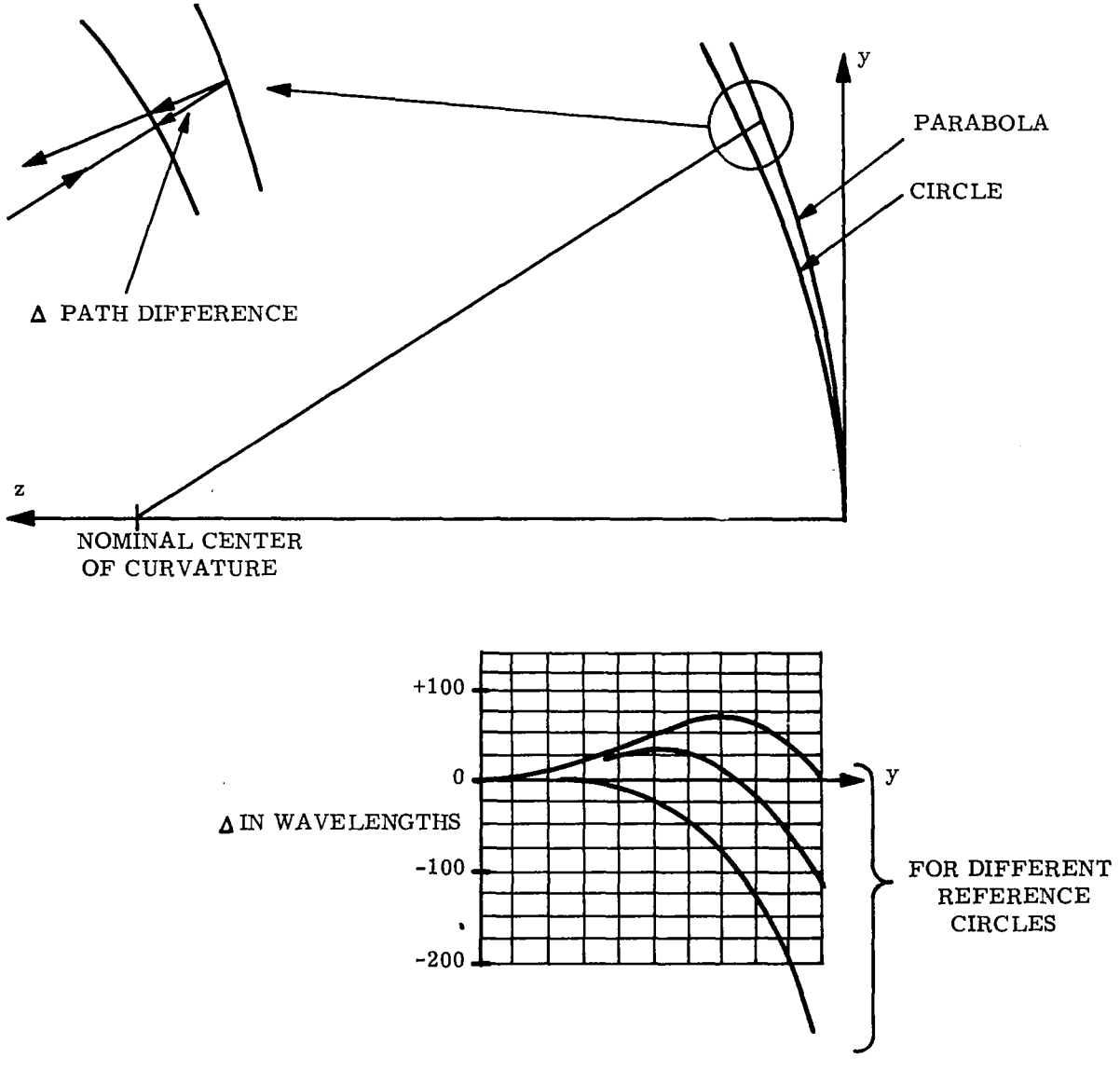

Figure 6. Aspheric Measurement Problem

which the fringe pattern generated by the actual "Δ path difference" is correlated with a reference pattern which is computed on the basis of a perfect optical element under test. Figure 7 shows how the correlation product is obtained. For simplicity, plane reflectors were used in preparing this figure.

Figure 8 shows a calculated and measured fringe pattern for an 8-inch f/1 parabola. Figure 8(c) shows a moiré pattern obtained by correlating (a) and (b). The residual fringe pattern is due to the fact that geometric distortion in a field lens was neglected in the computation. It was shown by laboratory demonstration that a moiré pattern can be used with the electronic phase measuring technique. Thus, a complicated aspheric reflecting surface can be measured by a real-time figure sensor.

Figure 9 shows the optical portions of the breadboard figure sensor set up to test the 8-inch parabola. Figure 10 shows the recommended optical arrangement for a "working model" of this type of figure sensor.

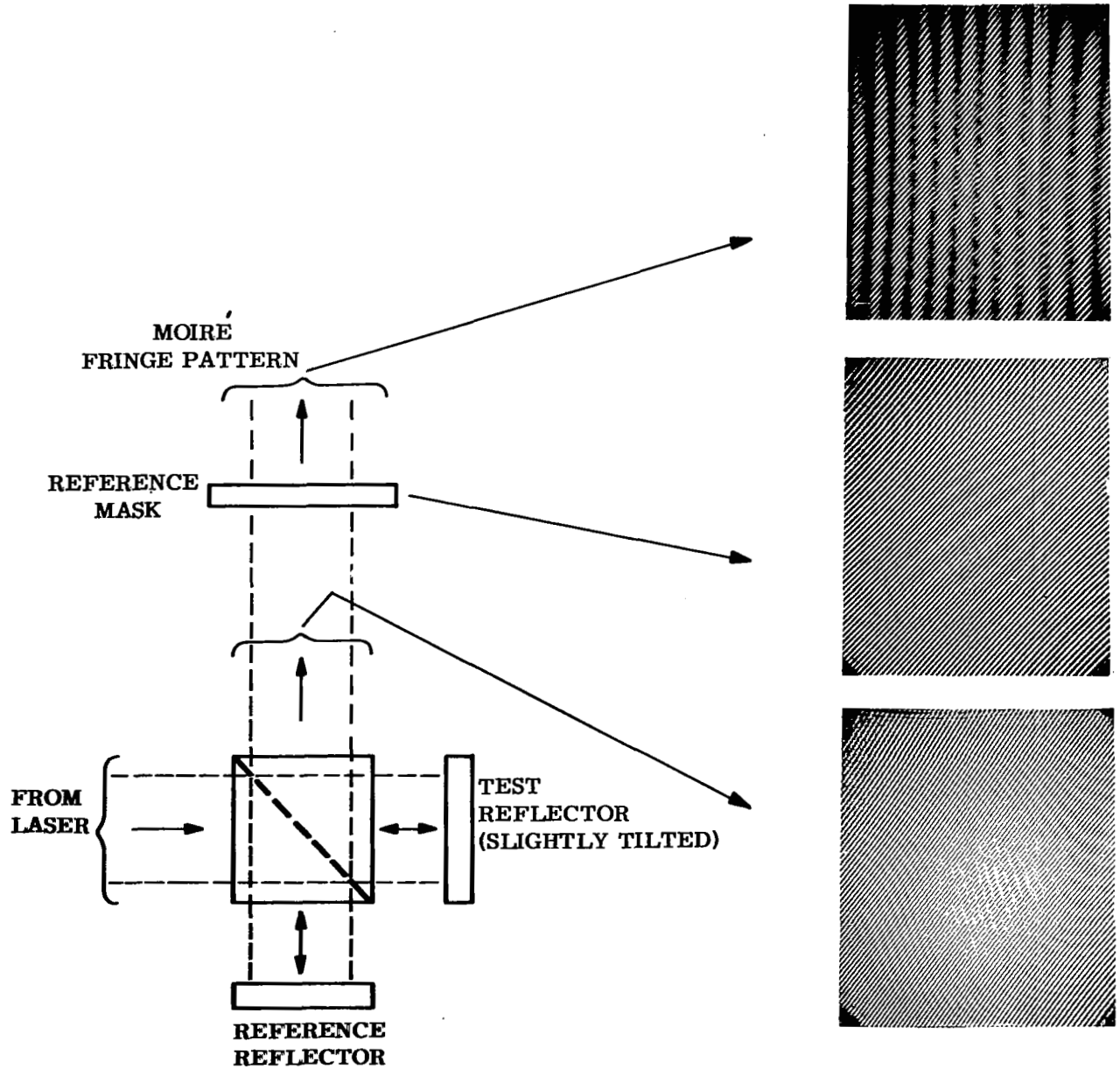

Figure 7. Moiré Pattern Analysis Approach

(a)

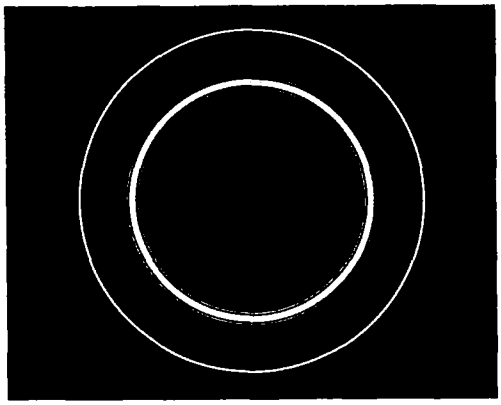

(b)

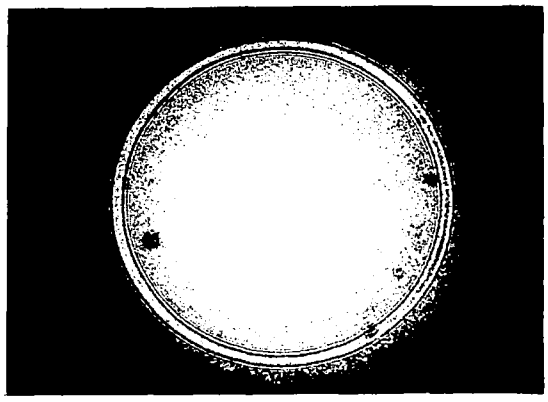

(c)

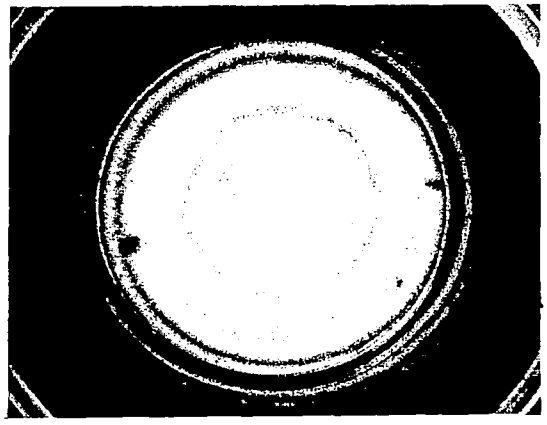

(d)

Figure 8. Fringe Patterns

(a) Reference Fringe pattern made from the calculated difference between a sphere and a parabola.

(b) Actual Fringe pattern measured from the difference between an f/1 parabola and a reference spherical mirror.

(c) Moiré pattern obtained from multiplication of actual pattern and calculated pattern.

(d) Moiré pattern similar to (c) above, but with the reference reflector tilted slightly.

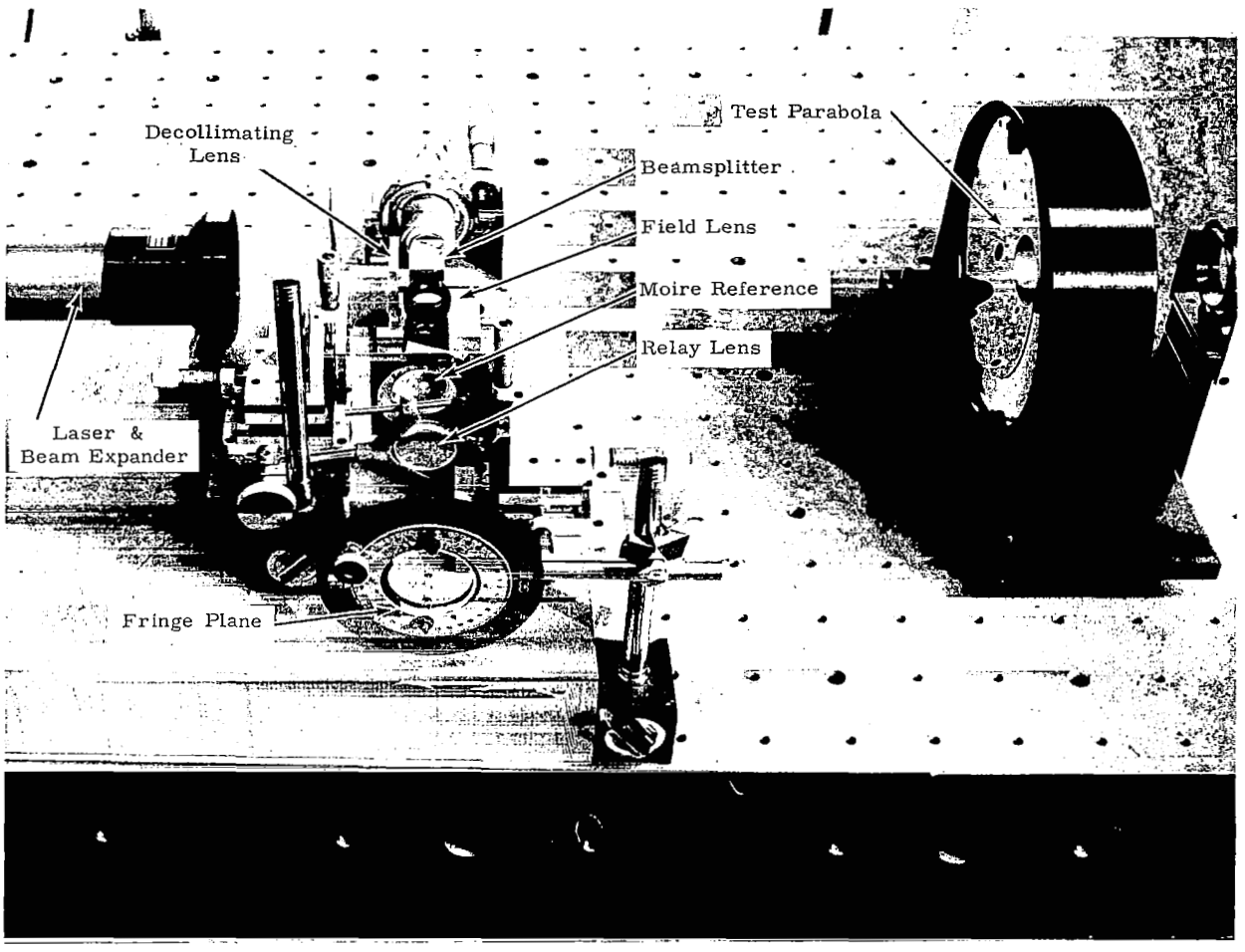

Figure 9. Breadboard Model of the Advanced Figure Sensor

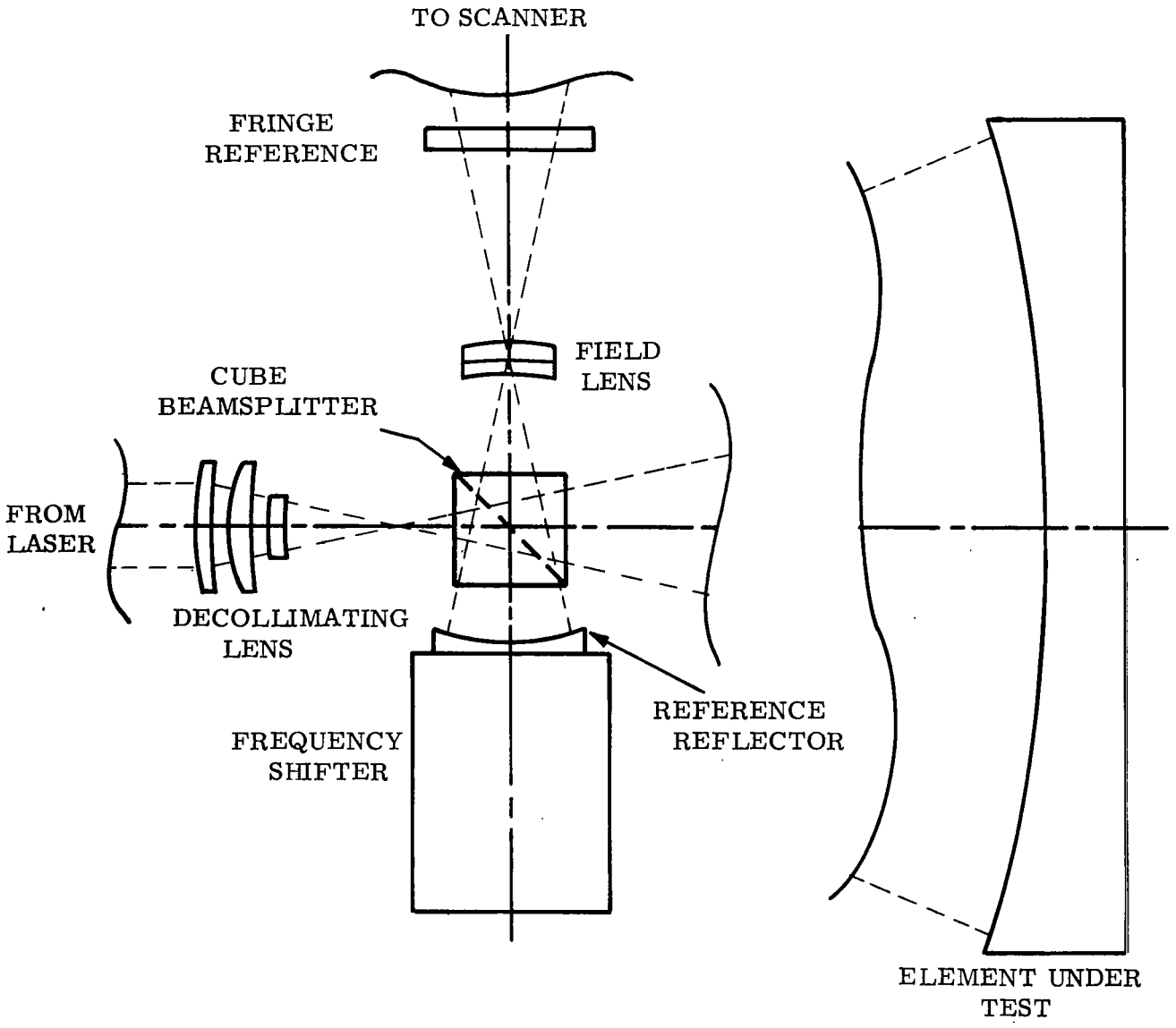

Figure 10. Recommended Interferometer Arrangement

3. FREQUENCY SHIFTER

Two approaches were investigated for the solid-state frequency shifter:

(1) Doppler frequency shift by axial translation of a reference reflector.

(2) Rotating 1/4 λ plate in circularly polarized light, where rotating 1/4 λ effect is produced by a rotating compression stress wave in an electro-acoustic-optical device.

The Doppler approach was selected because it is simple and was demonstrated to work well.

3.1 Doppler Frequency Shifter

The Doppler frequency shifter operates in the reference arm of the interferometer as shown previously in Figure 5. The frequency of the optical beam is shifted by moving the reference mirror in a direction parallel to the optical axis. Motion towards the beamsplitter increases frequency, and motion away decreases frequency according to

$$\Delta f = 2 \frac{u}{\lambda} \cos\theta \qquad (1)$$

Where:

Δf = frequency shift (sec^{-1})

u = mirror velocity (mm sec^{-1})

λ = optical wavelength (mm)

θ = angle of incidence relative to the velocity vector (deg)

Reasonably linear motion is required so that the electronic carrier frequency will be constant. The motion must also be bidirectional. Therefore, a triangular waveform was selected for the position-versus-time function. A total excursion greater than 1 wavelength is needed so that several cycles of carrier frequency will be generated. This is necessary for the electronic detector to operate properly. The present design is based upon 7 1/2 wavelengths per cycle of mirror motion.

The mirror surface should be maintained close to normal to the optical axis for all positions. Approximately $\lambda/20$ of tilt across the illuminated

portion of the reference mirror during the sweep will reduce the linear range of the sensor from ± $\lambda/4$ to ± $\lambda/4.5$. This effect is explained in paragraph 3.2. In addition, the Doppler frequency shifter must use no mechanically rotating parts or friction interfaces, and must be stable for long periods of time. Also very little power should be dissipated in the device or be required to drive it.

Characteristics of a breadboard frequency shifter are listed in Table I. For this model, a piezoelectric electro-mechanical transducer was selected because it is simple, requires no mechanical moving parts, and is mechanically rugged, and the required excursions can be obtained with reasonable drive voltages. Previous experience with actuators has shown that the most desirable transducer configuration is one in which all forces result in only compression or tension stresses, with no bending stress. Two transducer shapes were considered; a stack of thin wafers and a thin wall cylinder. The cylinder was selected because the axial symmetry causes only compression stress and does not cause bending stress in the mirror or in the supporting mount. A thin wall is desirable because it gives greater axial expansion for a given applied voltage than a thick wall. Electrodes are plated on the inner and outer walls of the cylinder so that the electrical potential is applied across the wall thickness. It was found that commercial grade piezoelectric material was not sufficiently homogeneous. Therefore portions of the inner wall electrode were isolated to allow use of compensating differential voltages. In this way, all sides of the cylinder should expand by the same amount, to give pure axial translation without mirror tilt. This compensation scheme helped but did not work as well as was hoped. The piezoelectric cylinders made from PZT-5 material were purchased from Clevite.

The piezoelectric material is quite stiff, having a Young's modulus comparable to that of glass. It was therefore necessary to find a mounting arrangement that would hold the mirror tightly within the end of the cylinder but would not allow cylinder exercising to squeeze the mirror. A simple Teflon cushion between the piezoelectric element and the mirror was found to work quite satisfactorily. Teflon has a Young's Modulus approximately 10 times smaller than that of either the transducer or the mirror. The cushion has a tight fit around the mirror circumference and is held within the end of

TABLE I

DOPPLER FREQUENCY SHIFTER CHARACTERISTICS

Frequency Shift	± 500 Hz
Axial Displacement of Mirror	± 2λ peak
Displacement Waveform	Triangular at 33-1/2 Hz
Clear Aperture	15 mm dia.
Mirror Tilt	< λ/20 peak to peak
Figure Error	< λ/100 peak
Internal Dissipation	1/4 watt

the transducer by a spring and slot arrangement. (See Figure 11.) The transducer is held in a mounting block by a set of Teflon-tipped setscrews. Calculations showed that the compressive forces conducted through the Teflon would cause less than $\lambda/500$ spherical aberration in the mirror.

The electronic circuit required to drive the transducer is relatively simple. Choice of frequency is bounded at low frequencies by the need to generate a carrier frequency greater than 120 Hz to avoid interference from the first harmonic of the power line frequency, and at high frequencies by the fact that the piezoelectric element presents a high capacity load. The selected cylinders have a capacity of 0.018 μF. A drive frequency of 33-1/3 Hz was selected with a sweep magnitude to produce 7-1/2 cycles per excursion or 15 cycles per drive period. This generates a signal carrier frequency of 500 Hz. A triangular motion waveform is preferred over a saw-tooth waveform because of hysteretic effects in the PZT-5 material. Figure 12 shows a block diagram of the high voltage drive circuit used for the breadboard tests.

3.2 Electronic Phase Detector

Two electronic signals are produced by two photodiodes placed in the interferometer output fringe plane. Electronic circuits are needed to detect the relative phase of these two carriers.

A new circuit was designed and used in the breadboard tests to give a linear range of ± 180 degrees, compared to ± 90-degree linear range for previous circuits.

The circuit schematic is shown in Figure 13. The signal and reference carriers from photodetectors are fed to a pair of limiters to reject amplitude noise. A bridged Zener diode in the feedback loop of the operational amplifier produces hard limiting and sharp axis-crossing transitions. The reference carrier is inverted, i.e., shifted in phase by 180 degrees, relative to the signal carrier. Both waveforms are further sharpened by a pair of differentiating networks so that a short pulse is produced for each axis crossing. The negative-going pulses trigger a binary flip-flop. The output of the flip-flop can be considered as a positive gate with duty cycle proportional to phase difference between the signal and reference carriers. This variable width

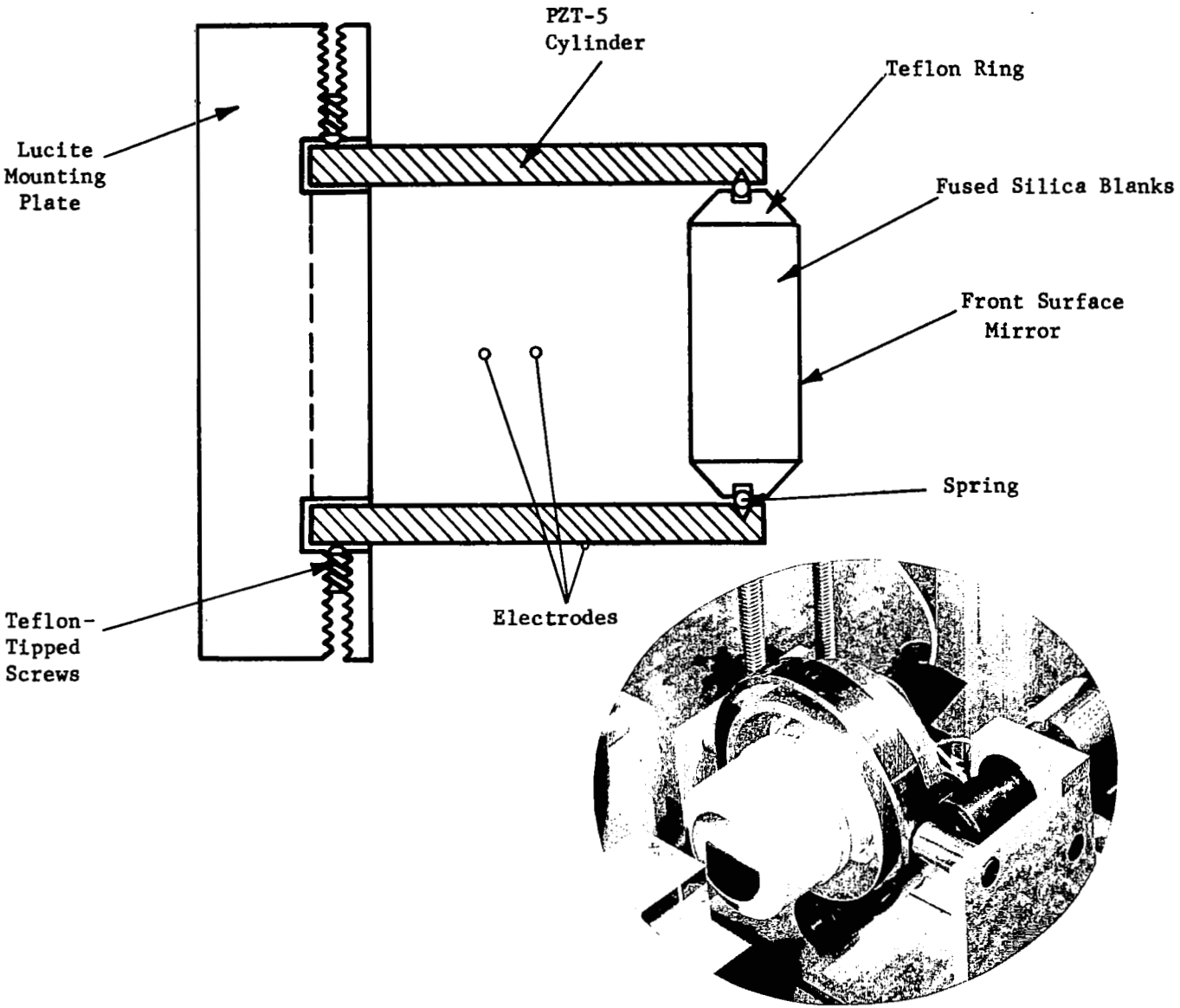

Figure 11. Doppler Frequency Shifter Mechanical Assembly

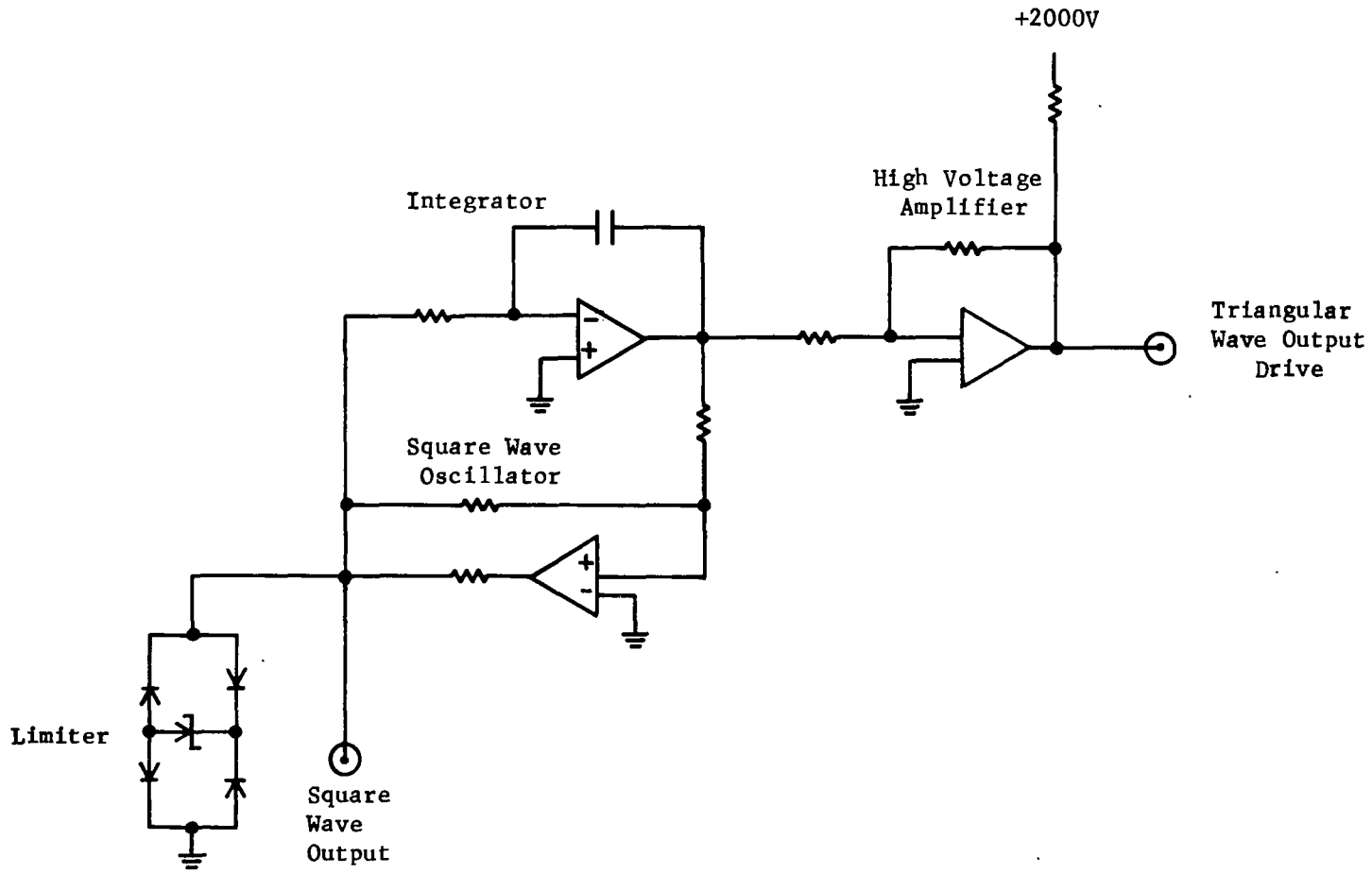

Figure 12. Doppler Frequency Shifter Drive Generator Circuit

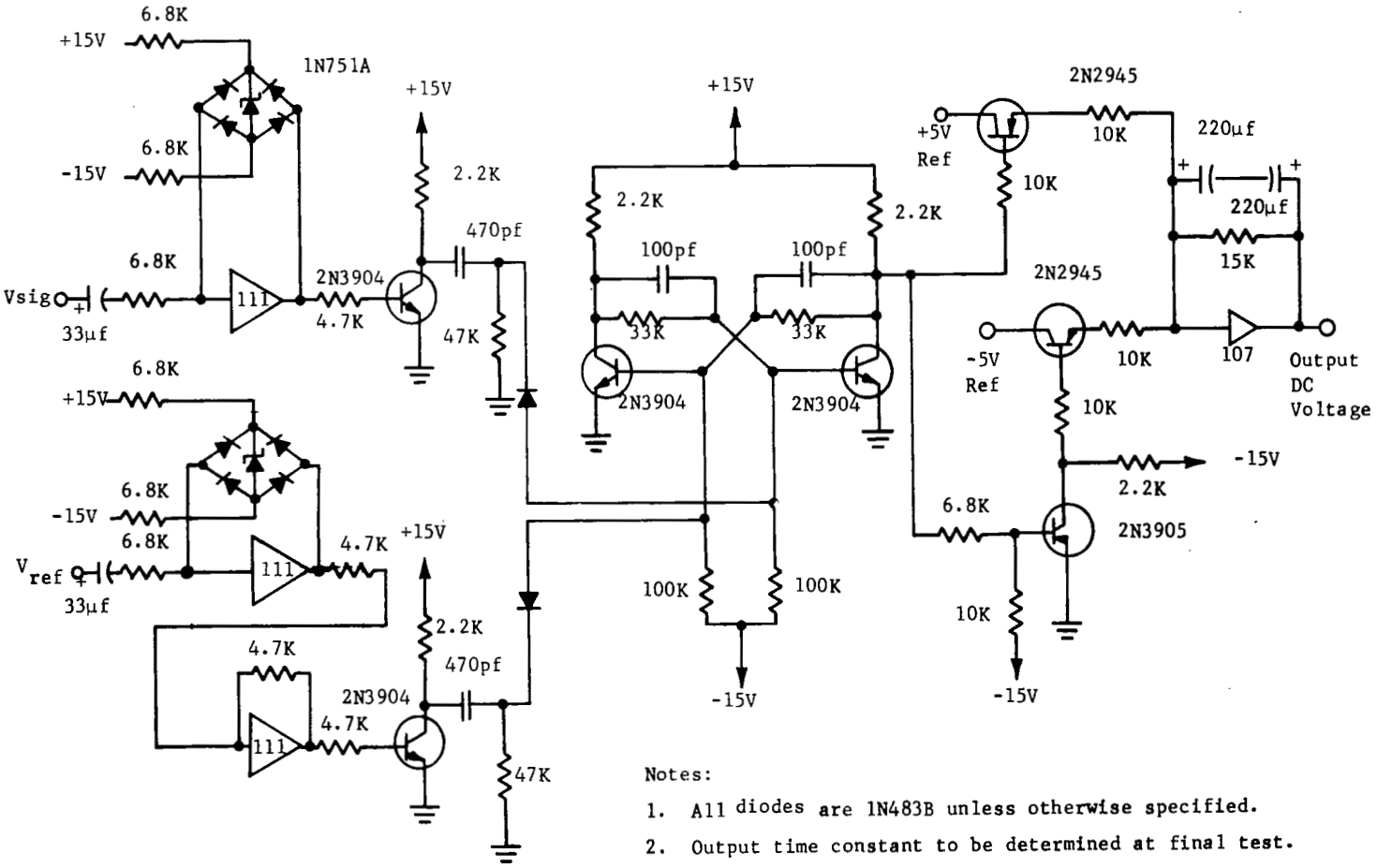

Figure 13. ±180° Linear Phase Demodulator Schematic

gate then controls two transistor switches that feed plus and minus reference voltages to a summing and integrating amplifier.

The measured relationship between phase difference and output dc voltage is very linear over phase angles of ± 180 degrees as shown in Figure 14. Changes in output with 10-percent variation of power supply voltages were undetectable. Input carrier voltages greater than 100 mv rms cause no change in the output. Similarly, this circuit is independent of input carrier frequency in the range from 10 Hz to 2 kHz.

When this phase detector is applied to the figure sensor, it is necessary to know how the calibration curve will be affected by the imperfections of the actual signals to be handled. These imperfections will include noise, spurious signals, changes in carrier level, changes in carrier frequency, and frequency modulation of one carrier relative to the other due to mirror tilt in the Doppler frequency shifter.

Amplitude changes and amplitude noise will not pass through the hard limiters. Changes in frequency of both carriers between 10 Hz and 2 kHz have been shown to have no effect. Relative frequency modulation and phase noise will cause degradation. The predominant effect for small changes will be a loss in linear range, with no effect on accuracy. If the Doppler shifter is adjusted for ± 2λ deviation, i.e., 8 cycles of carrier per deviation excursion, the equation for the phase detector output is:

$$V_{dc} = \frac{E_{dc}}{1440} \sum_{n=\pm(1,2,3,4)} \left\{\theta + \frac{n}{4}\gamma\right\} \qquad \text{when } -180 < \left\{\ \right\} < +180$$

or

$$\left\{\theta + \frac{n}{4}\gamma - 360\right\} \qquad \text{when } \left\{\ \right\} > +180$$

or

$$\left\{\theta + \frac{n}{4}\gamma + 360\right\} \qquad \text{when } \left\{\ \right\} < -180$$

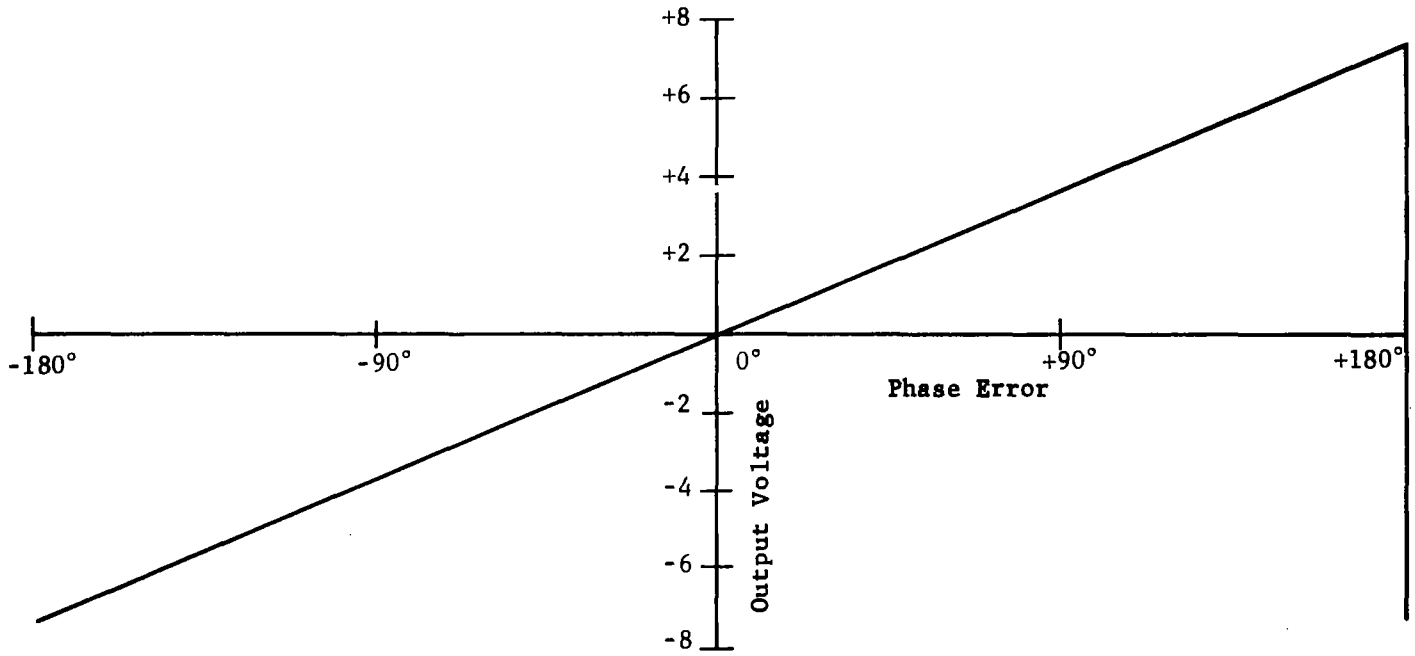

Figure 14. Transfer Characteristics of ±180° Linear Phase Demodulator

Where:

E_{dc} = maximum dc voltage

θ = phase error due to figure error (deg)

γ = random phase modulation due to carrier frequency modulation or noise or mirror tilt (deg peak)

This equation is plotted in Figure 15 for one polarity of figure error only.

When the phase detector circuit is used with the Doppler frequency shifter, three features must be added to accommodate the following factors:

(1) For a fixed figure error, the carrier phase error changes polarity each time the Doppler frequency shift changes polarity. To compensate for this, the output dc polarity is reversed in synchronism with the driver sweep.

(2) The piezoelectric material has significant hysteresis; i.e., the mechanical sweep lags behind the applied drive voltage. This effect is accommodated by blanking off the phase detector for 3 milliseconds following each sweep reversal.

(3) For certain conditions, the signal and reference carriers may contain a different number of axis-crossings, causing ambiguous output voltage. This is corrected by an "and" gate synchronized with the sweep reversals.

The phase detector circuit with these additions is shown in block form in Figure 16. Typical waveforms throughout the electronics are shown in Figure 17. Letters in Figure 16 identify locations at which these waveforms are found.

Overall performance of the figure sensor using a Doppler frequency shifter is shown in Figure 18. This is a recording of the output DC voltage as a function of differential optical path difference in one half of one beam of the interferometer. The recording was obtained by placing a thin piece of mica in one half of one beam. The mica was then rotated about an axis perpendicular to the beam. This produced a slowly changing OPD in that portion of the beam. A reference detector monitored the undisturbed portion of the beam and

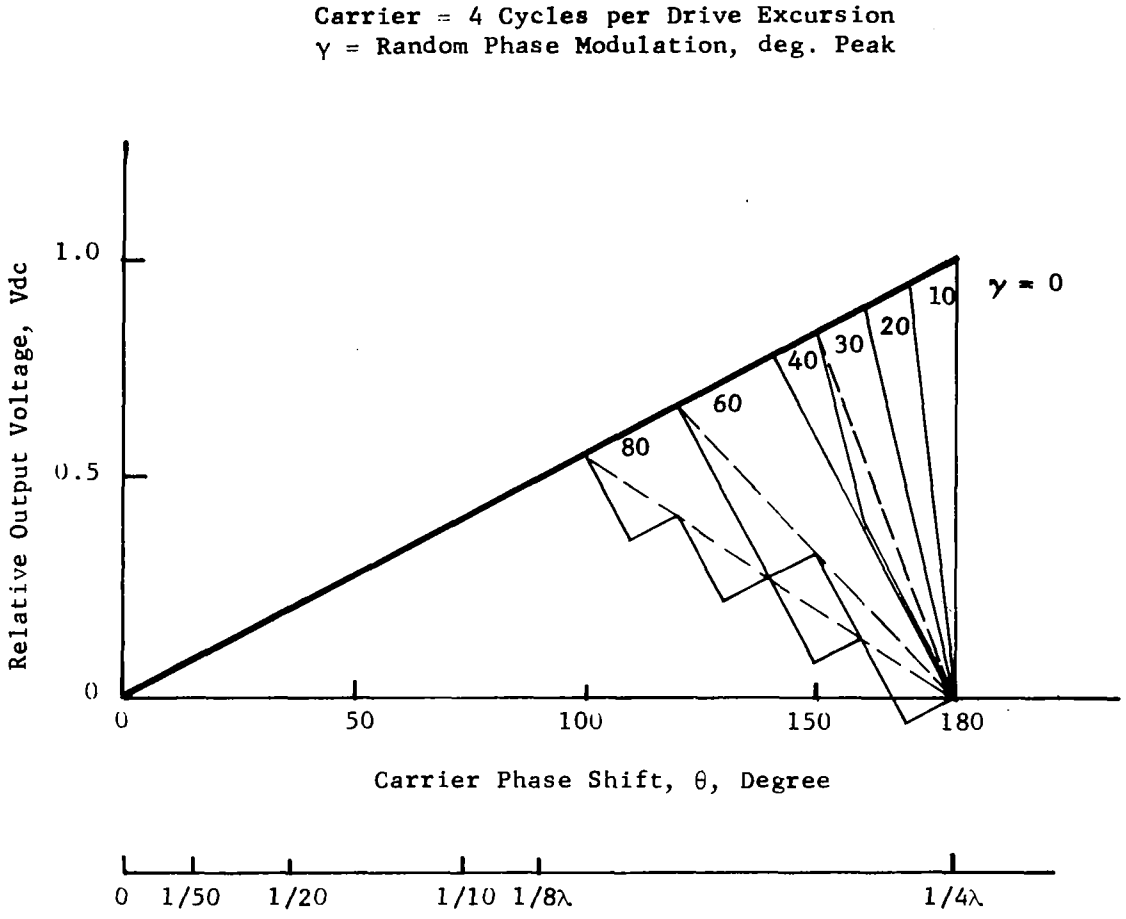

Figure 15. Calculated Transfer Characteristic of Electronic Phase Detector

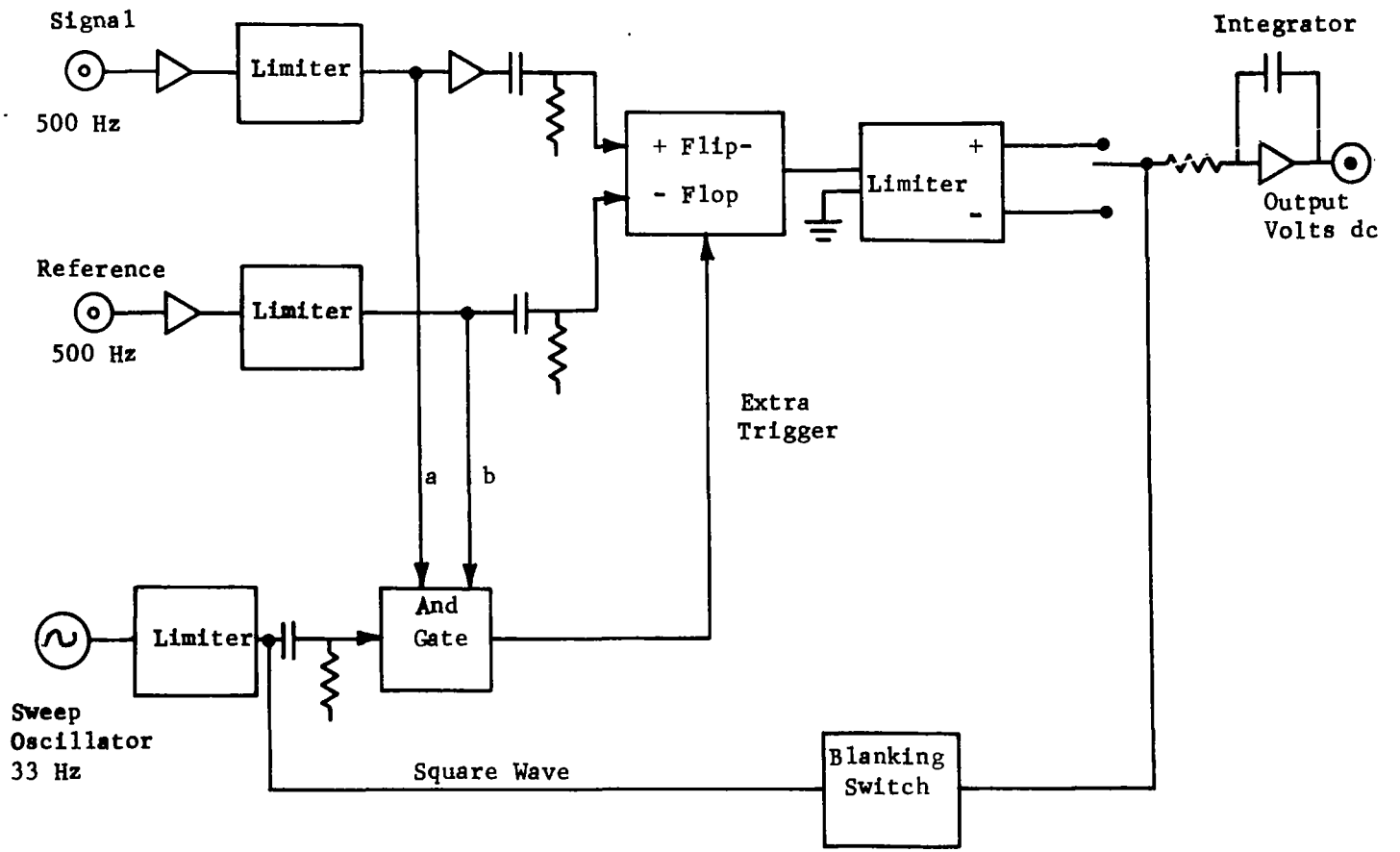

Note: Letters Refer to Waveforms of Figure 17

Figure 16. Block Diagram of Phase Detector Electronics

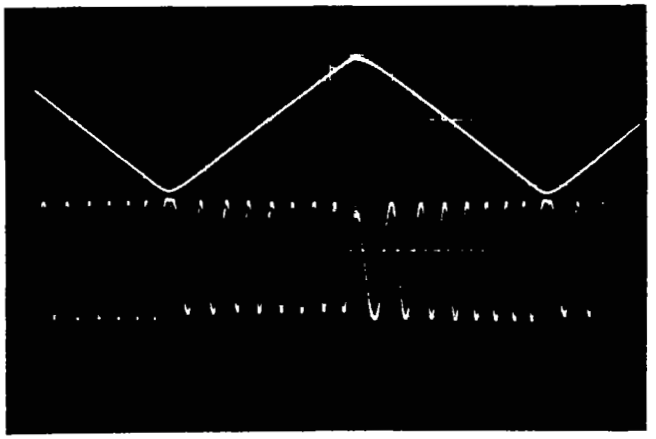

(a) Top: Frequency Shifter Drive (Point "a")
Bottom: Preamplifier Carrier Output (Point "b")

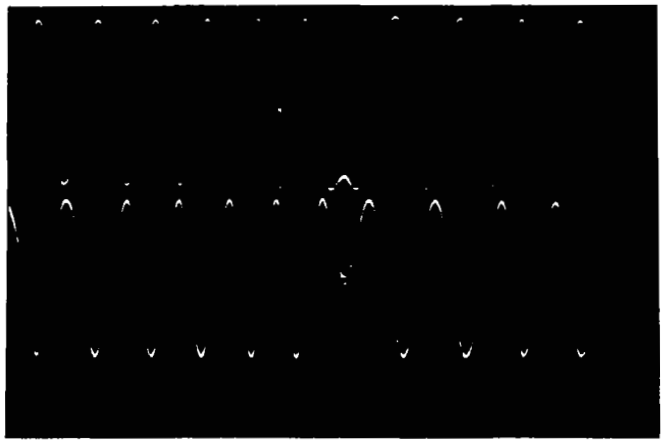

(b) Top: Signal Carrier (Point "c") with large figure error of approx. $\lambda/4$
Bottom: Reference Carrier (Point "d")

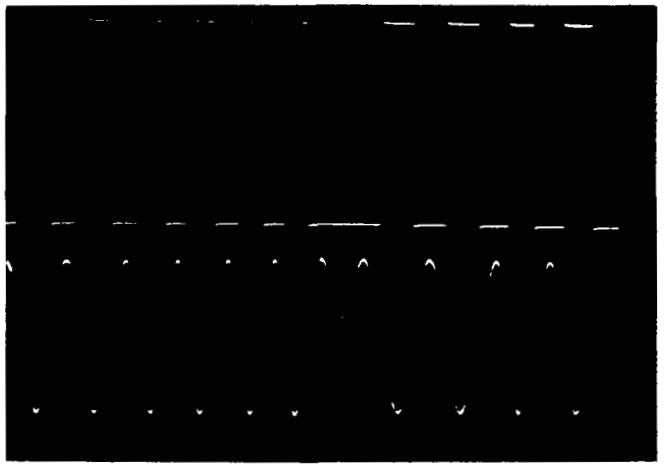

(c) Top: Limiter Output (Point "e")
Bottom: Signal Carrier (Point "c")

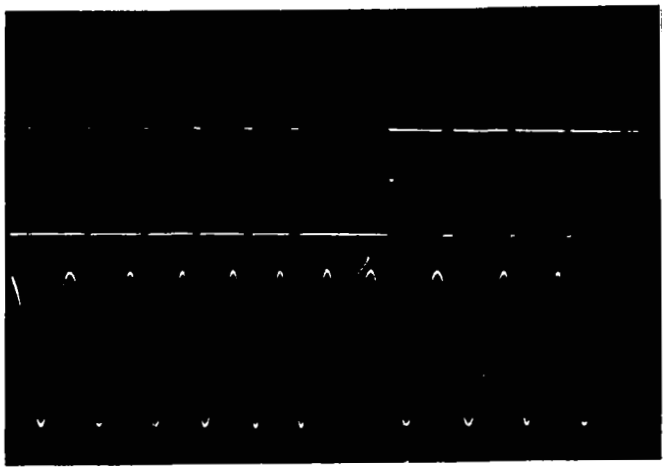

(d) Top: Multivibrator Output (Point "f") with large figure error
Bottom: Signal Carrier (Point "c")

Figure 17. Electronic Waveforms (See Figure 16 for Point Locations)

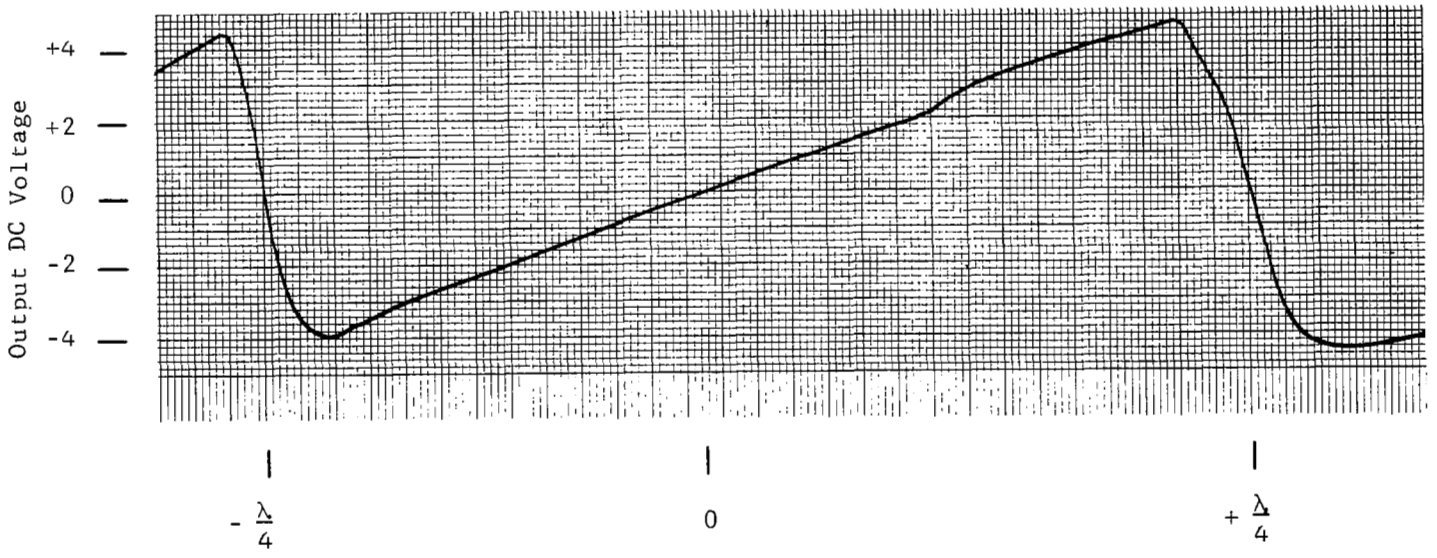

Figure 18. Breadboard Figure Sensor Calibration

the second detector monitored the disturbed portion. An overall response bandwidth of 5 hz was used.

3.3 Rotating 1/4 Wave Plate

The second approach to building an optical frequency shifter is one in which a combination of fixed and rotating 1/4 λ plates are placed in the reference beam. The beam passes through these elements twice to produce 360 degrees of delay for every 180 degrees of rotation of the rotating 1/4 λ plate. Operation of this device can best be understood by considering a vector diagram of the wave train as it passes through the elements for one particular orientation of the rotating 1/4 λ plate. Let the input wave be represented by a vector  which can be resolved into orthogonal components  and passed through a 1/4 λ plate, oriented with its optical axis parallel to one of the components  . At the output of the 1/4 λ plate, the component in parallel with the optical axis is delayed 90 degrees relative to the perpendicular component. This may be represented by  where the numerals refer to relative phase retardation of the marked vector. These vectors can again be resolved into  plus 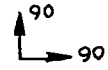 and passed through a second 1/4 λ plate oriented vertically , producing 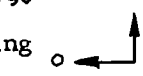 plus 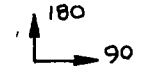 . The wave train is now reflected from a fixed reflector, reversing all vectors by 180 degrees and producing 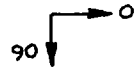 plus 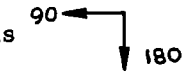 The vectors are again passed through the second 1/4 λ plate, still oriented vertically  , to produce 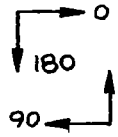 plus  , which is equivalent to 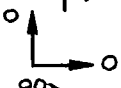 plus . These can be summed to give  and  , which are then passed through the first 1/4 λ plate, oriented at 45 degrees  . This produces  and  which can be summed as  . Thus, the input vector has been operated upon to produce an output vector with the original polarization but delayed in phase by 90 degrees.

As the orientation of the second 1/4 λ plate is rotated, this delay changes, going from zero to 360 degrees delay for each 180 degrees of rotation. If the second 1/4 λ plate is rotated at a constant rate of 1 cycle per second, the coherent light passing into and back out of this arm of interferometer is shifted in frequency by 2 cycles per second. It can be shown that the same device can produce the same overall effect when combined with a polarization-sensitive element in the interferometer output arm.

One objective of the project was to evaluate the application of a solid-state rotating 1/4 λ plate for the frequency shifter. This device is an electronically driven element, optically equivalent to a mechanically rotated 1/4 λ plate. It consists of a fused silica disk that is mechanically stressed by piezoelectric transducers. Several transducers are mounted around the edge of the disk and excited by an ac voltage. By proper control of the excitation amplitude and phase, it is possible to generate a rotating stress wave in the glass. This causes a rotation of the birefringence axes in the glass.

One of the many mechanical modes of oscillation that can be excited in a disk is illustrated in Figure 19(a). If a cyclic force is applied at F_1, vibrations will occur with excursions as shown by the dotted lines. Because of the nature of solid material, it is not possible to excite a vibration in one axis only; all three dimensions determine the mode characteristics. The desired mode has equal x and y dimensions, with a smaller z dimension. Incremental elements on the x and y axes are subject to radial motion only; and incremental elements on ± 45° axes are subject to tangential motion only. Therefore, a second independent, or orthogonal, mode can be induced by a cyclic force at 45° as shown by F_2 in Figure 19(b). By proper adjustment of the relative phase of F_1 and F_2, i.e., by adjustment of $\phi = \frac{\pi}{4}$, it is possible to generate a compression stress that effectively rotates about the z axis at the frequency w. (See Figure 19(c).)

In mathematical terms, the birefringence is equal to (Ref. 7)

$$R_t = Ct\,(p-q) \qquad (2)$$

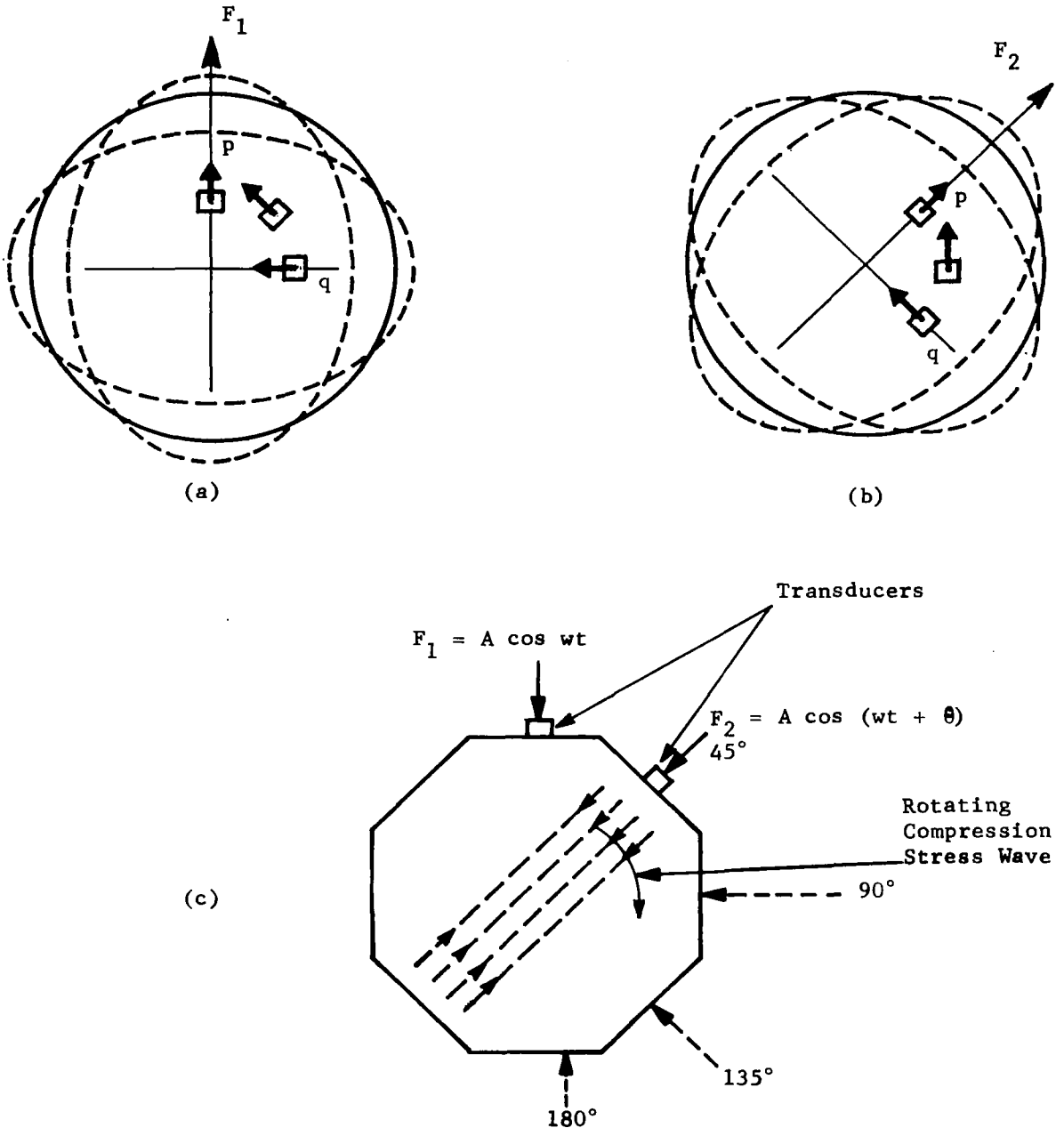

Figure 19. Acoustical Resonate Modes In a Thick Disk

Where:

C = stress-optic coefficient

t = thickness of plate

p and q = principal stresses

R_t = ratio of index of refraction for fast and slow axes

By definition, the principal stresses are in planes free from shear, at right angles to each other, and are respectively the greatest and smallest of all normal stresses in the element (Ref. 7). The slow and fast optical birefringence axes are parallel to the principal stress axes, p and q. Since the birefringence effect is sensitive to stress magnitude and not polarity, the birefringence axes rotate at the frequency 2ω.

An experimental model of a solid-state rotating 1/4 λ plate was made by Perkin-Elmer prior to the start of this project (Ref. 1). This model had two shortcomings: the useful aperture was severely limited, and alignment and operation of the unit were very difficult. A second model was made to solve these problems (see Figure 20). Flat sides were used in the second model to give a more uniform stress distribution over the clear aperture and to isolate the two modes for ease of alignment. Also, the force transducers were mounted on the glass disk edge instead of on the face to increase the aperture. These approaches were successful for one mode, but there was still a severe difficulty with the second mode.

Both original and second models used three-phase excitation, and it is now believed that this accounts for the critical alignment problem. Work on this approach was stopped after the Doppler frequency shifter was found to work successfully.

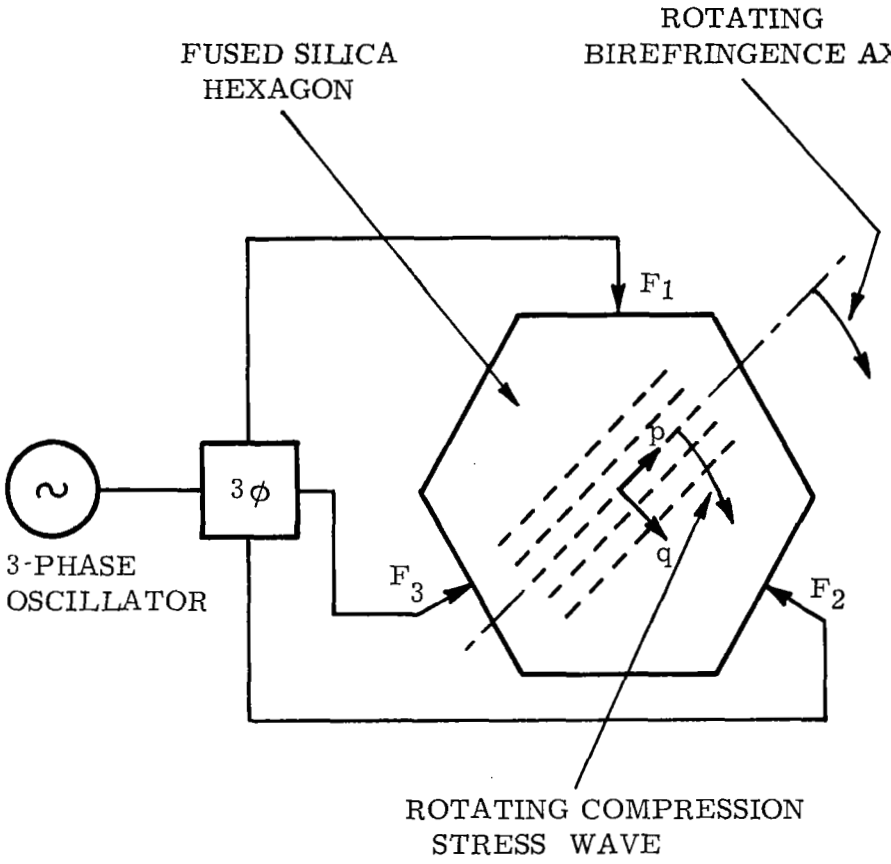

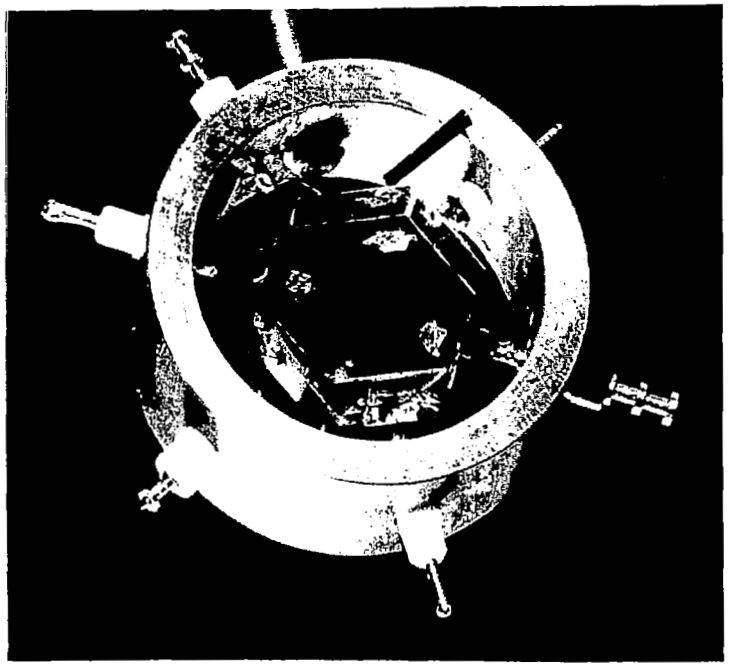

BIREFRINGENCE α $F_p - F_q$

Figure 20. Experimental Solid-State Rotating 1/4 λ Plate

4. ASPHERIC MEASUREMENT

4.1 Problem and Approaches

The present concept for the application of a figure sensor in an active optics telescope system requires the sensor to measure the primary mirror from its center of curvature rather than from the prime focus. Since the primary mirror figure will undoubtedly be other than spherical, the figure sensor must therefore measure aspheric surfaces from the vicinity of the paraxial center of curvature. The specific project objective was to measure an 8-inch, f/1 parabola.

Measurement of a parabola presents two problems:

(1) When the parabola is illuminated by a diverging bundle of rays, all emanating from the paraxial center of curvature, most of the return rays cross the optical axis somewhere other than at the paraxial center. (See Figure 21.) This may be stated in different terms: Different zones of the parabola are concentric about different points on the optical axis; that is, normals to the parabola surface cross the optical axis at different points. The spread between the axis crossings of the paraxial normals and the edge ray normals may be called longitudinal spherical aberration. For the 8-inch f/1 parabola, the longitudinal spherical aberration is 12-1/2 mm. (See Figure 22.)

(2) The optical path length from the nominal center of curvature and back is not the same for all zones. The approximate difference between a parabola and a sphere is shown in Figure 23 by a plot of the axial or z-axis displacement of a parabola from a sphere as a function of radial dimension, y, in the pupil plane.

Three approaches were investigated to find a solution to these problems. These utilized:

(1) An aspheric reference reflector to generate wavefront distortions that match those due to the difference between a parabola and a sphere as shown by Figure 23.

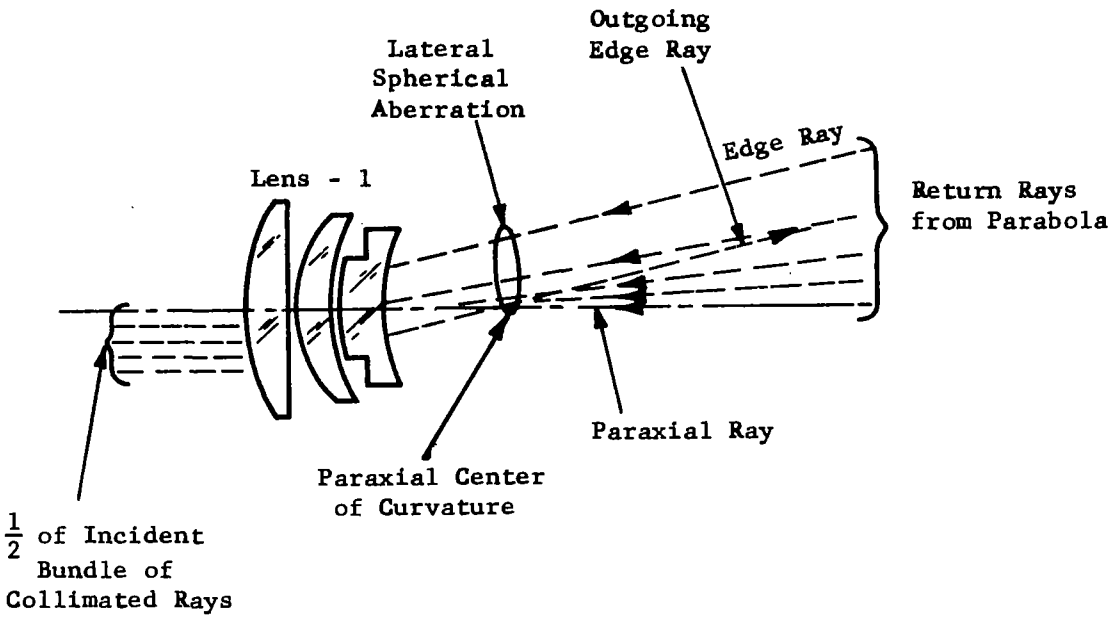

Figure 21. Spherical Aberration of a Parabola When Illuminated From its Center of Curvature

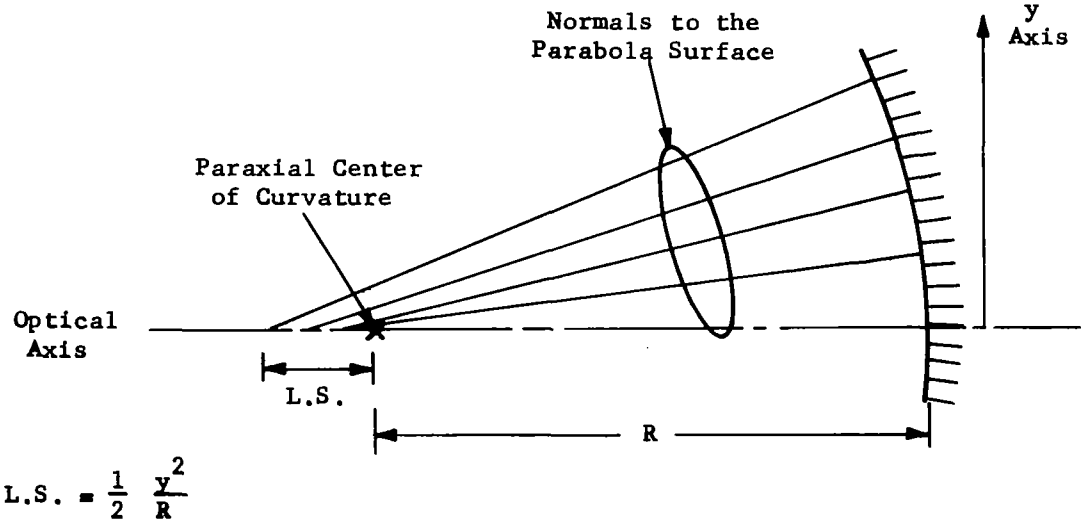

Figure 22. Locus of Intersection of Normals to a Parabola with the Parabola Axis

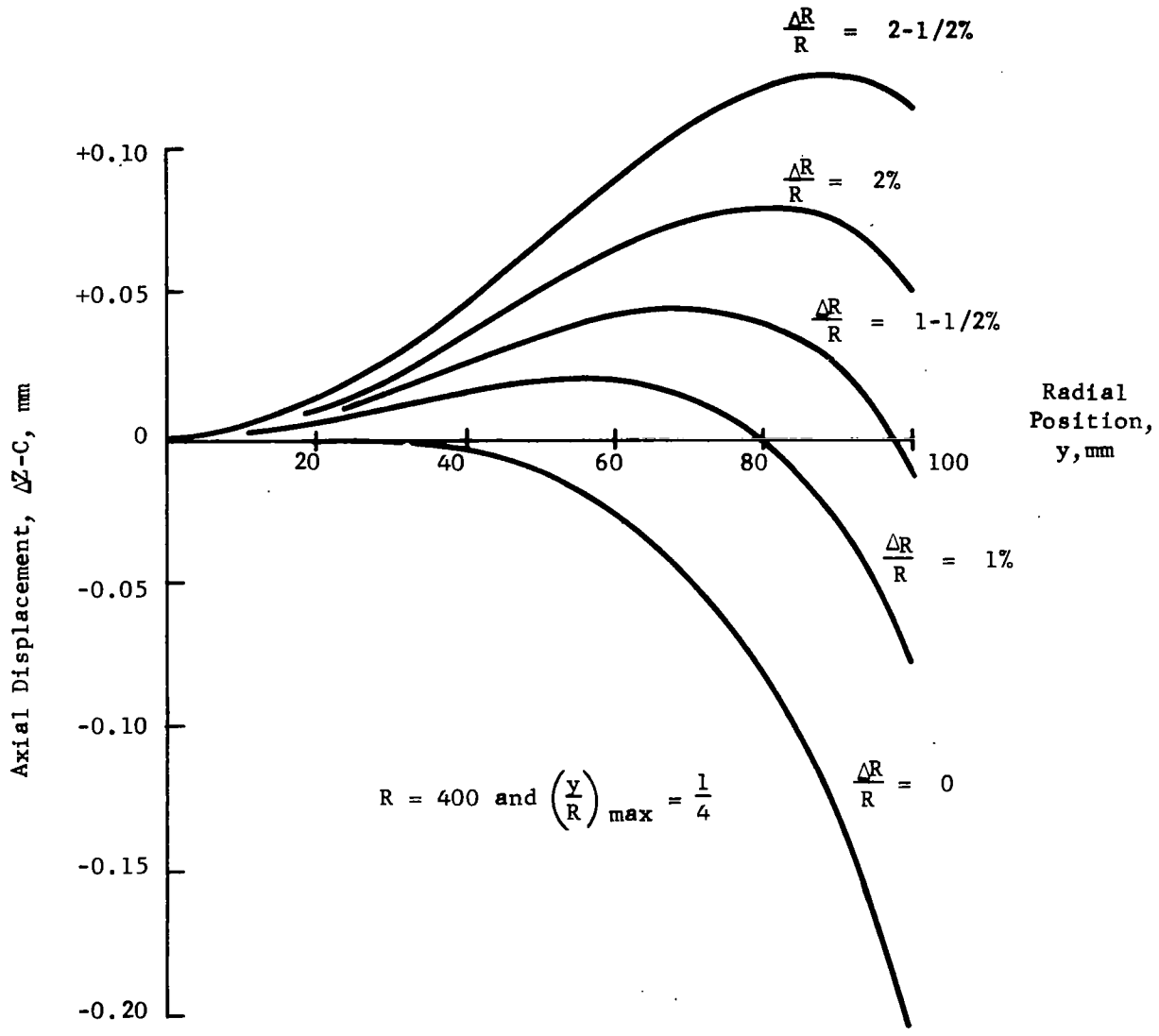

Figure 23. Z-Axis Displacement of a Parabola from a Sphere

(2) A null corrector in place of Lens-1 (see Figure 2 for identification) to generate spherical aberrations matching those found when viewing a parabola from its center of curvature, as described by Figure 22.

(3) Moiré interference pattern analysis of the interference pattern resulting from the optical path difference due to the difference between the test parabola and a spherical reference reflector.

The aspheric reference approach is feasible and simple in principle, but the reference element itself was found to be exceedingly difficult to fabricate.

Two null correctors were designed, one with three elements and one with four. The best that could be done using spherical elements only was to reduce the overall optical path difference to approximately 8 waves.

The moiré interference pattern analysis was demonstrated to work with plane and spherical mirrors. Calculations indicate that is should also work well with the 8-inch parabola, and that the technique is equally applicable to much larger mirrors. Therefore the moiré analysis approach was selected for the 8-inch parabola measurement.

Moiré analysis of an 8-inch, f/1 parabola represents the same degree of difficulty, with regard to the number of fringes that must be handled, as a 120-inch, f/2 parabola. Therefore, this is believed to be a valid test in terms of the eventual application. It should also be pointed out that the moire analysis method also provides a simple mechanism by which figure errors in the figure sensor optics may be corrected.

The conclusion which may be drawn from this work is that the moire analysis may be used in combination with the electronic phase measuring technique to measure the figure of a fast parabola.

4.2 Aspheric Reference Reflector

Figure 24 shows the physical arrangement of the interferometer with an aspherical reference element. In this figure Lens-1 images the parabola at a plane "p" located a little over 20 mm to the left of Lens-1 and a distance "l" from the beamsplitter. The reference reflector is also located the same

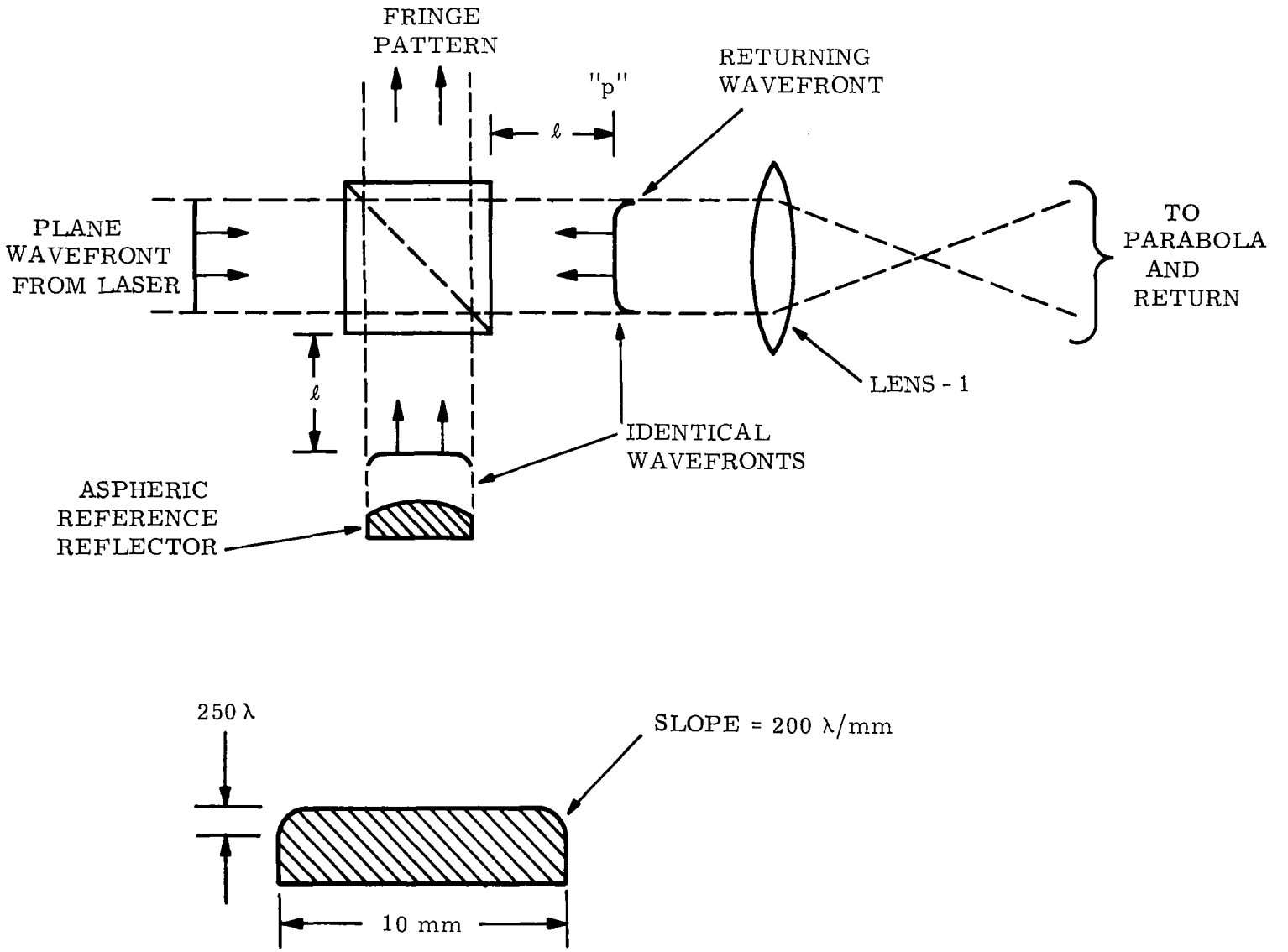

Figure 24. Aspheric Reference Reflector Approach

distance "1" from the beamsplitter. The returning wavefront at plane "p" will contain distortions caused by the parabola. The aspheric reflector must produce a duplicate distorted wavefront. The required reference reflector surface contour will now be calculated.

Because Lens-1 illuminates the parabola with a spherical wavefront, we are concerned only with the difference between the parabola and a sphere. Furthermore, the choice of radius for the sphere is an independent variable. For the geometry of Figure 25 we may write the equation of a parabola as

$$z_p = \frac{1}{2}\left(\frac{y}{R}\right)^2 R,$$

and the equations for a circle as

$$z_c = \frac{1}{2}\left(\frac{y}{R}\right)^2 R + \frac{1}{8}\left(\frac{y}{R}\right)^4 R + \frac{1}{16}\left(\frac{y}{R}\right)^6 R + \ldots\ldots,$$

and for the difference between two circles of different radii as

$$\Delta z_c = -\frac{1}{2}\left(\frac{\Delta R}{R}\right)\left(\frac{y}{R}\right)^2 R - \ldots\ldots$$

where:

z = displacement in the z dimension away from the y axis (z axis coincides with the parabola optical axis)

y = radial dimension in the pupil plane ($2y_{max}$=parabola diameter)

R = parabola paraxial radius of curvature

The equation for the difference between a parabola and a sphere then becomes

$$\Delta z = +C - \frac{1}{2}\left(\frac{\Delta R}{R}\right)\left(\frac{y}{R}\right)^2 R + \frac{1}{8}\left(\frac{y}{R}\right)^4 R + \frac{1}{16}\left(\frac{y}{R}\right)^6 R \qquad (3)$$

where:

C = a constant displacement in the z direction

This is the equation used to prepare Figure 23 with R = 400 mm.

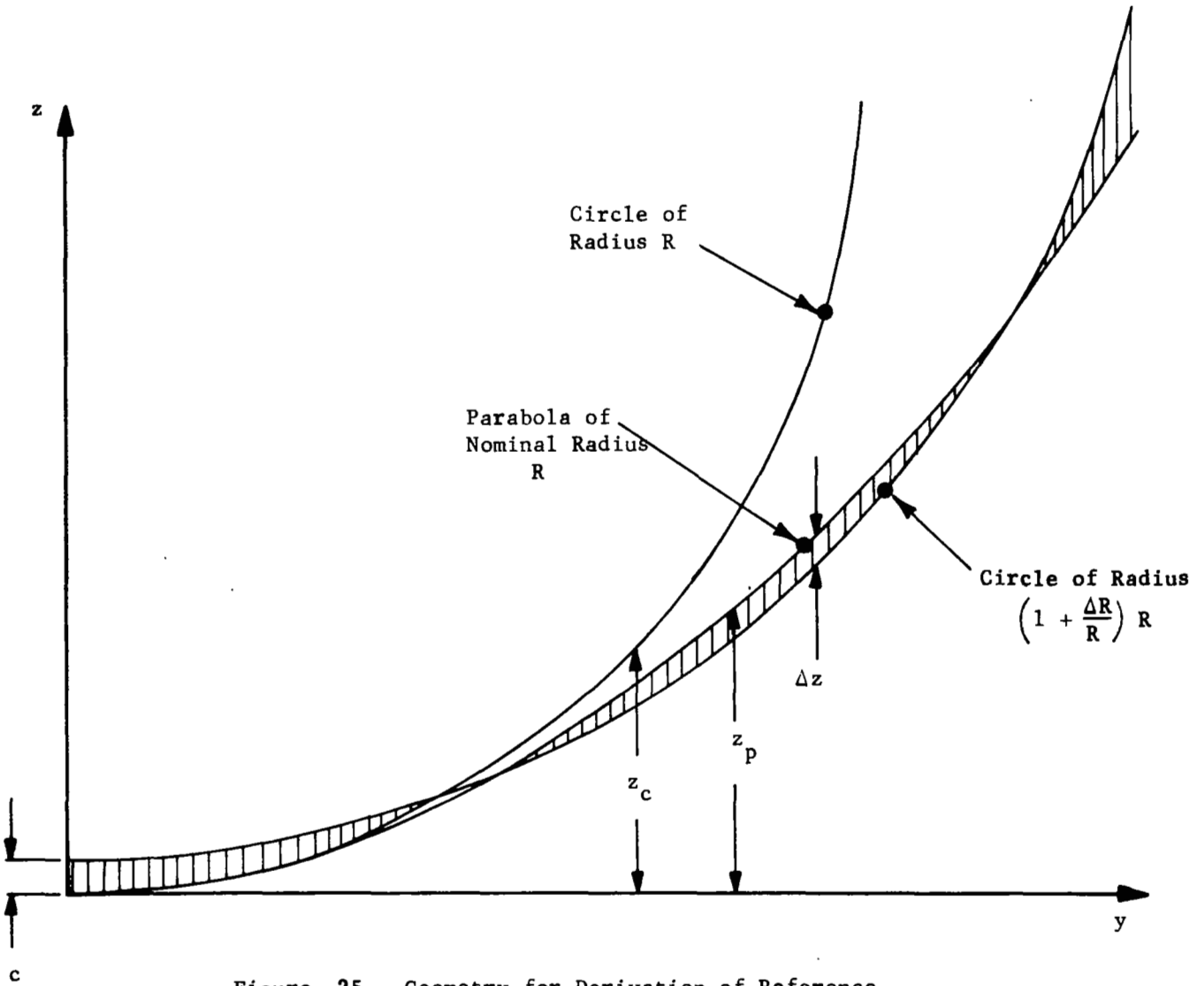

Figure 25. Geometry for Derivation of Reference Reflector Equation

We may disregard C because we are only interested in changes in optical path as a function of ray position in the y plane. Also if we let

$$R = 400 \text{ mm}$$

$$\frac{\Delta R}{R} = 0.02$$

then:

$$|\Delta z| = 4\left(\frac{y}{R}\right)^2 - 50\left(\frac{y}{R}\right)^4 - 25\left(\frac{y}{R}\right)^6 \text{ (mm)}$$

This equation may be divided into its spherical and aspherical parts:

$$|\Delta z| = \underbrace{\left[4\left(\frac{y}{R}\right)^2 + \left(\frac{y}{R}\right)^4 + \frac{1}{2}\left(\frac{y}{R}\right)^6\right]}_{\text{Spherical Part}} - \underbrace{\left[51\left(\frac{y}{R}\right)^4 + 25\tfrac{1}{2}\left(\frac{y}{R}\right)^6\right]}_{\text{Aspherical Part}} \text{ (mm)} \qquad (4)$$

If the reference reflector is the same size as the interferometer beam, the diameter will be 10 mm. The spherical part can be generated on a mirror of this diameter by a spherical convex figure with a radius of curvature of 8 mm. This part is easy to make.

The difficult part to fabricate is the aspheric remainder in equation (4). This is predominantly a fourth power term where

$$|\Delta z| \times 50\left(\frac{y}{R}\right)^4 \text{ mm} \qquad (5)$$

for an f/1 parabola $\left|\frac{y}{R}\right|_{max} = 1/4$ and $(\Delta z)_{max} = 0.2$ mm.

Five different approaches were investigated for fabricating the curve defined by equation (5); none were successful.

Perhaps the most interesting approach was the attempt to generate this figure on a relatively thin tapered disk and with the edge one half as thick as the center. The disk was bent away from the polishing tool at the center by air pressure while it was being processed. Simple bending of an edge-supported disk with a uniformly distributed load produces a predominately second power curve, i.e., one that is close to a parabola. However, the stiffness of

a thin disk is proportional to the third power of its thickness; hence, the tapered thickness was intended to cause significantly more bending at the edge than at the middle. Figure 26 is a fringe pattern of the test piece before processing, showing the surface to be flat. Figure 27 is a fringe pattern of the same piece after the special processing. This shows the piece to be curved and slightly astigmatic. The shape of the curve, as indicated by this data, is shown in Figure 28 together with a calculated curve for a constant thickness disk. It can be seen that the effect of tapered thickness was disappointingly small.

4.3 Null Corrector

A null corrector is conventionally a set of optical elements inserted between an aspheric reflector and a test device to make the reflector appear to be spherical. A null corrector was used successfully in the final figuring of the Stratoscope II primary mirror (Ref. 8). Figure 22 has shown that a parabola viewed from its nominal center of curvature has a large amount of spherical aberration. The function of a null corrector is to generate the matching spherical aberration from ei .er a diverging or a collimated input bundle. (See Figure 29.)

Two null corrector designs were made: one with three elements and one with four elements. Only spherical surfaces were considered. Figure 30 shows the calculated overall optical path difference when the null correctors were mated with the 8-inch f/1 parabola. If an 8-inch parabola were the largest reflector to be tested, these designs could be corrected by use of aspheric surfaces. However, the magnitude of longitudinal spherical aberration increases linearly with the primary mirror size. This means that the 12 mm of aberration could become as large as 180 mm for a very large mirror; with the result that the null corrector elements would become quite large and involve a lot of glass in transmission.

Although the null corrector approach is certainly feasible, it was put aside in favor of the moire pattern analysis, which requires fewer optical elements in the interference beams. This was not a compelling decision and the use of a null corrector should continue to be considered in the future.

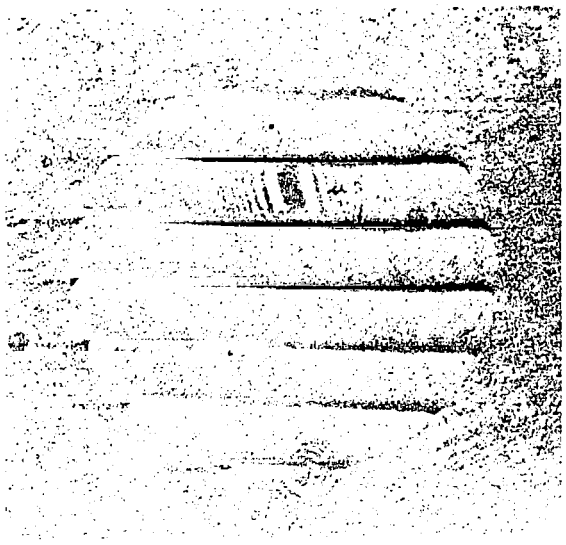

Figure 26. Fringe Pattern of Experimental Reference Reflector Blank Before Processing

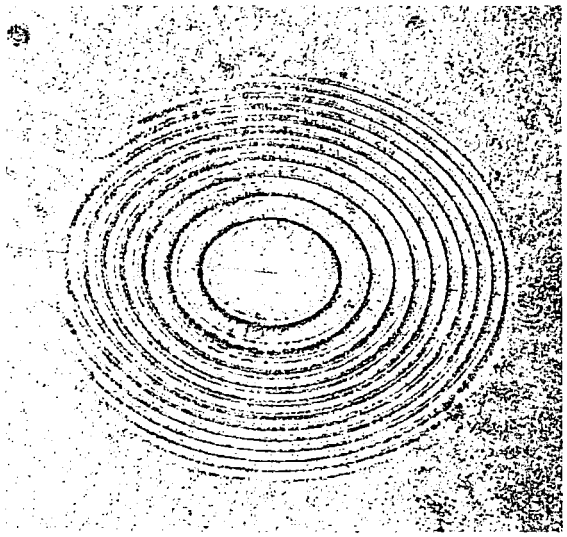

Figure 27. Fringe Pattern of Experimental Reference Reflector After Processing

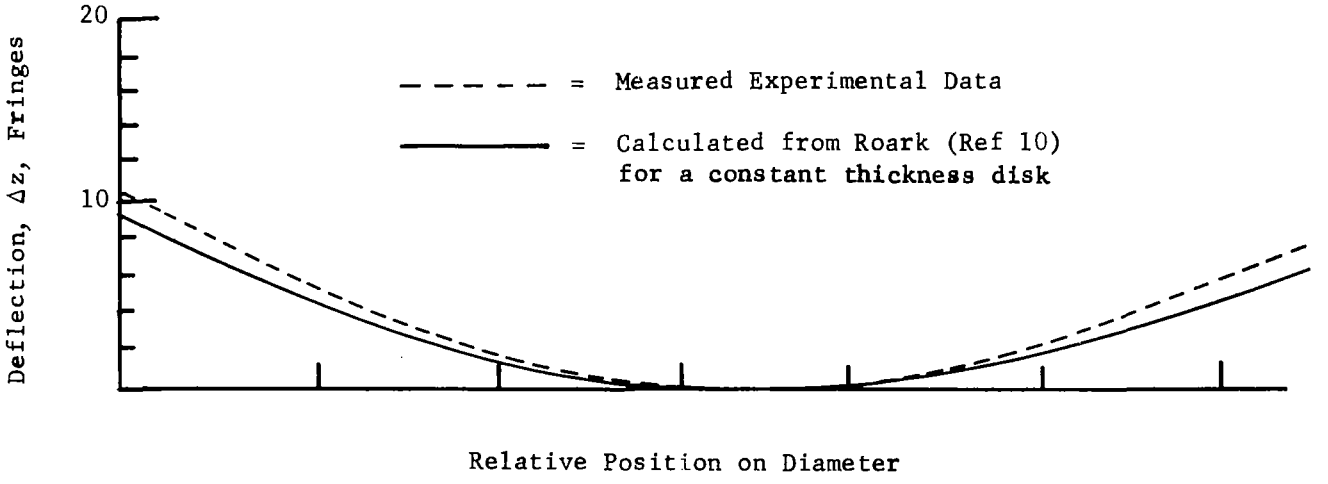

Figure 28. Comparison of Figure Generated by Special Processing With Calculated Bending of an Edge-Supported Disk of Constant Thickness by a Uniformly Distributed Load

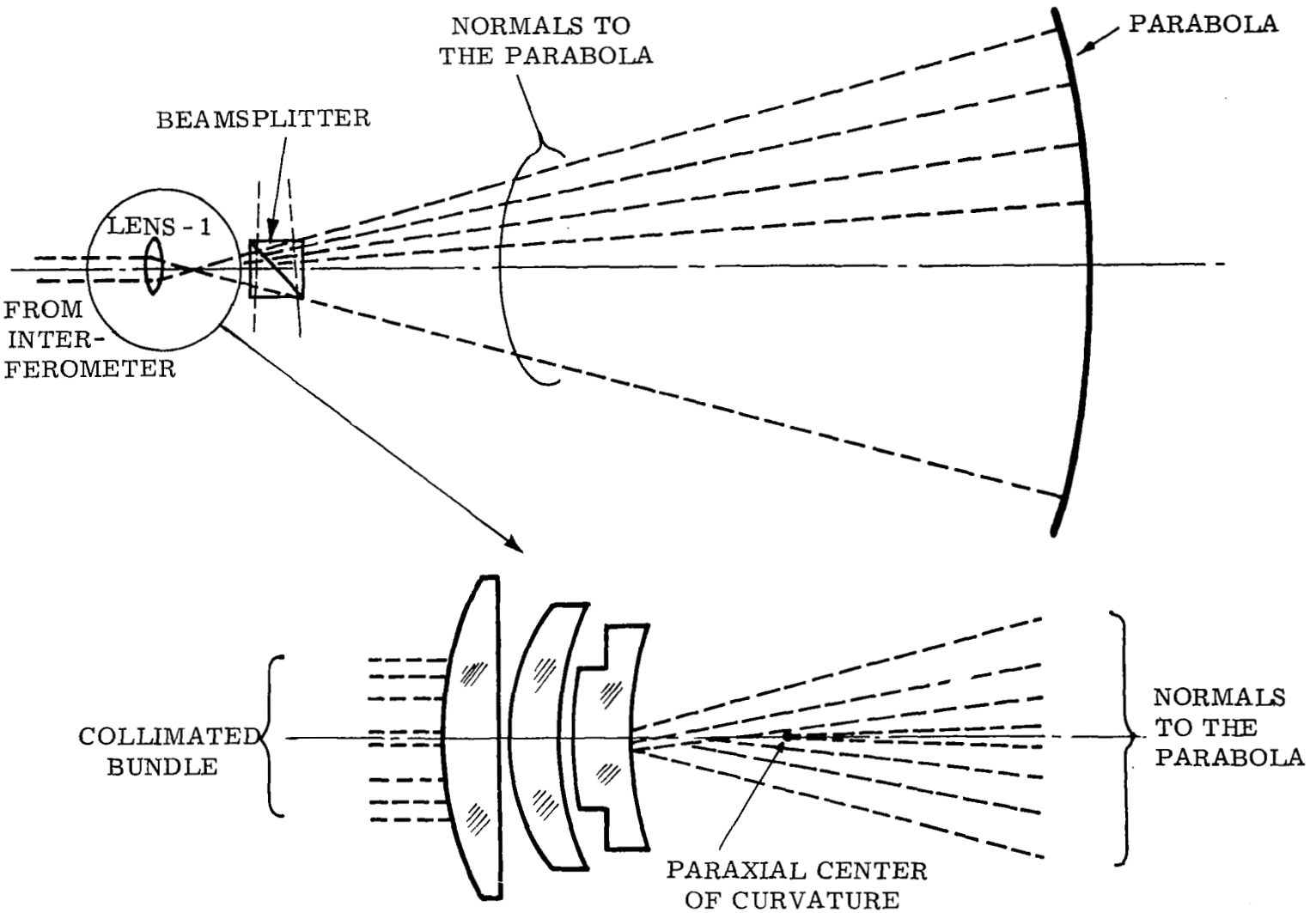

Figure 29. Null Corrector Approach

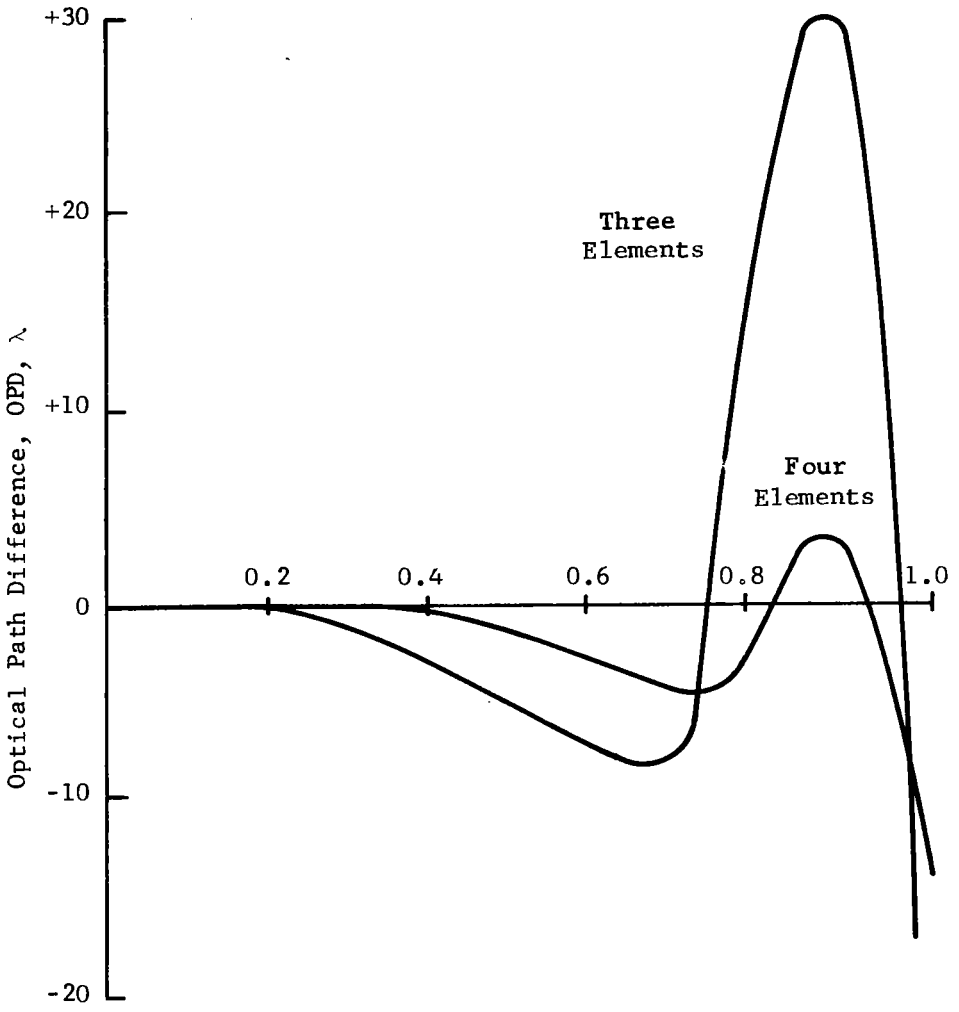

Figure 30. Calculated Optical Path Difference for Two Different Null Correctors Used With the f/1 Parabola

4.4 Moiré Pattern Analysis

Moiré patterns are well known, and many techniques employing them have been long established (Refs. 3, 9). Moiré patterns are usually produced by the superposition of two grids or line patterns. If one line pattern is an interferogram representative of an optical surface and the other an ideal master pattern, the resultant moiré pattern is also representative of the deviation of the optical surface from the ideal design. In many cases, complex interferogram patterns can be more easily interpreted by moiré pattern analysis.

The work performed for this project resulted in the successful combination of moiré pattern analysis with the automatic phase measuring technique. The advantages of this approach include: use of simpler optics in the interference beam paths, testing of aspheric elements, and cancelling out of figure errors in the interferometer components.

Figure 7 in Section 2 has shown the arrangement of optical components for this approach. For simplicity, this illustration was prepared with a line grid instead of a circular reference pattern. The interferometer fringe pattern was obtained with two plane mirrors, one of which was slightly tilted to produce the desired fringe frequency. The moire pattern is the two-dimensional product of the fringe pattern with a 100-line-per-inch Ronchi ruling.

Figure 31 shows a similar set of interference and moire patterns. However, in this case, one mirror has been translated axially in steps by means of the piezoelectric transducer. It can be seen that the fringes seem to "walk" up the page as voltage is applied to the transducer. Actually the pattern is changing phase as a function of transducer voltage, and hence as a function of reference reflector axial position. Thus, moiré patterns can be used with the phase measuring technique. Overall figure sensor calibrations similar to Figure 18 were also obtained using moiré pattern analysis.

A valid demonstration of the moiré fringe analysis technique applied to the measurement of an aspheric element should be done with a reference master fringe pattern which has been made from the theoretical design figure of the parabola, and with the moiré pattern obtained by a superposition of the actual fringe pattern upon the synthetic reference master.

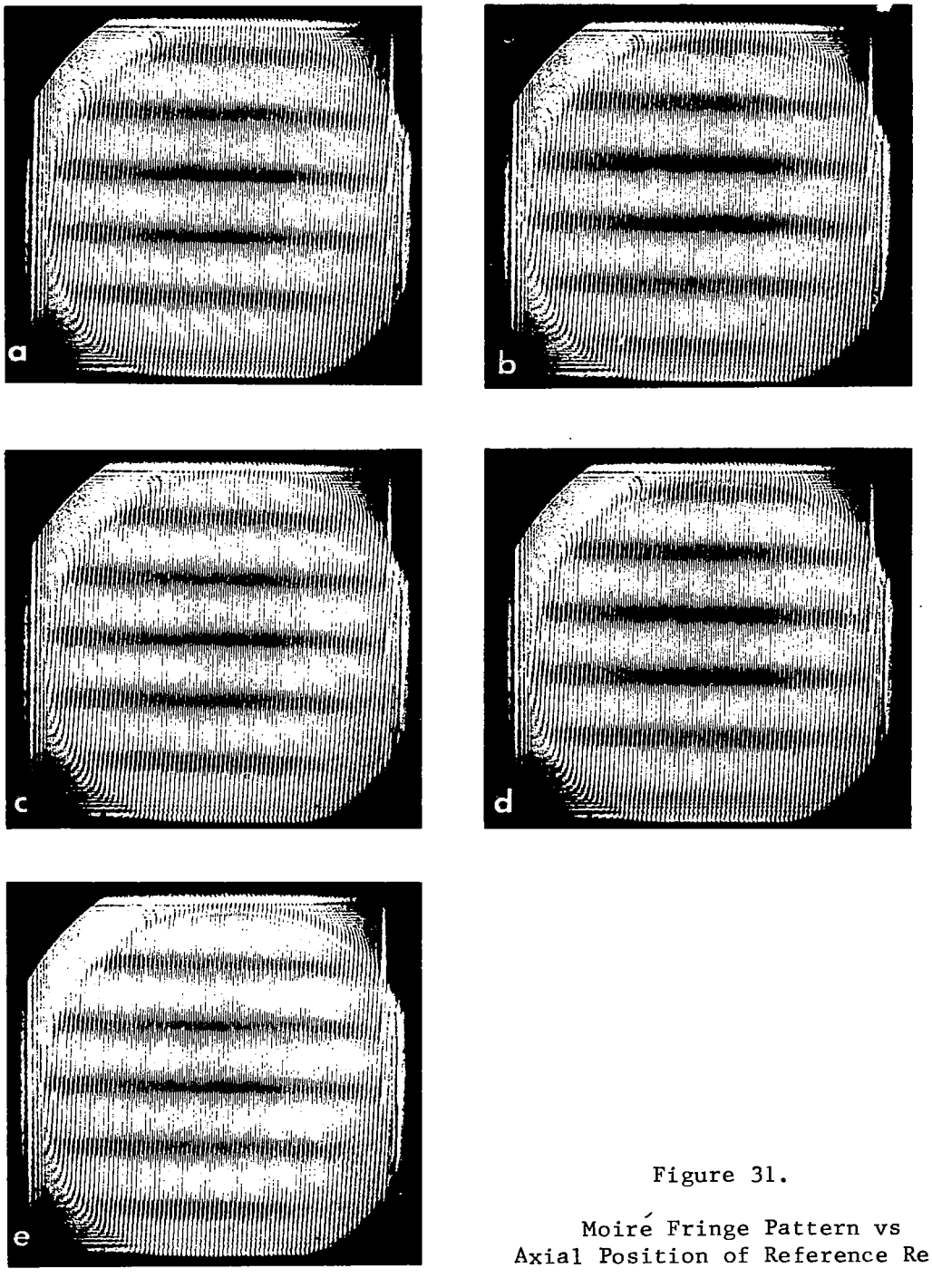

Figure 31.

Moiré Fringe Pattern vs
Axial Position of Reference Reflector

The computation of the reference master for the 8-inch f/1 parabola is based upon the geometry shown in Figure 32. In this figure the two interference beams superimposed, only the edge ray is shown, and the folding due to the beamsplitter is omitted. The point "C" is the focal point of Lens-1 and represents the point source of the interferometer illumination bundle. The interference pattern will be caused by the optical path difference, OPD, which is defined by:

$$OPD = \frac{(CDE - CAC) - (CHJ - CBC)}{\lambda} \qquad (6)$$

This OPD will vary as a function of θ, the ray elevation angle above the optical axis.

The calculation is complicated by the additional spherical aberration due to the beamsplitter cube. A comparison was made between this component of spherical aberration for the two beams; one to the spherical reflector and one to the parabola, each passing through the beamsplitter cube. The difference between the two was found to be approximately 0.25λ for the edge ray. A slight amount of defocusing could, in principle, reduce to less than $\lambda/20$ the maximum difference between the two beams due to the aberration. Therefore, it was decided to perform the first calculation neglecting the beamsplitter glass. A final calculation (for the design of a "working model" figure sensor) will include a complete ray trace from point "C" to the output fringe plane.

A program was worked out for the Hewlett-Packard Model 9100A Calculator based upon the geometry of Figure 33 and the following equations:

$$y_1 = \left\{ \frac{\left[1 + 2\,(1 + \delta)\,\tan^2\theta\right]^{1/2} - 1}{\tan\theta} \right\} R$$

$$sag = \frac{1}{2}\,\frac{(y_1)^2}{R}$$

$$\ell_1 = \frac{(1 + \delta)R - sag}{\cos\theta}$$

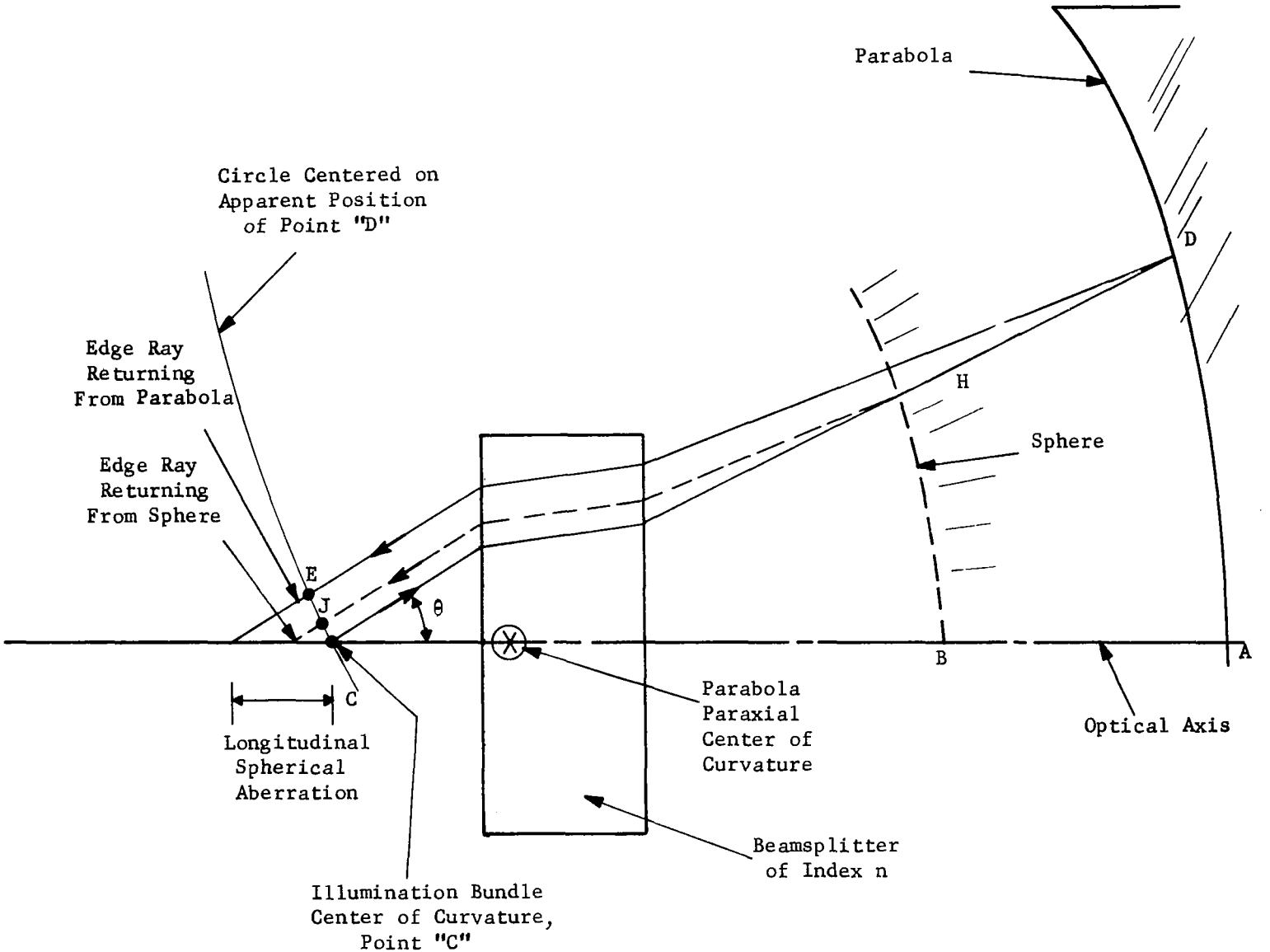

Figure 32. Geometry for Derivation of Moiré Reference Master

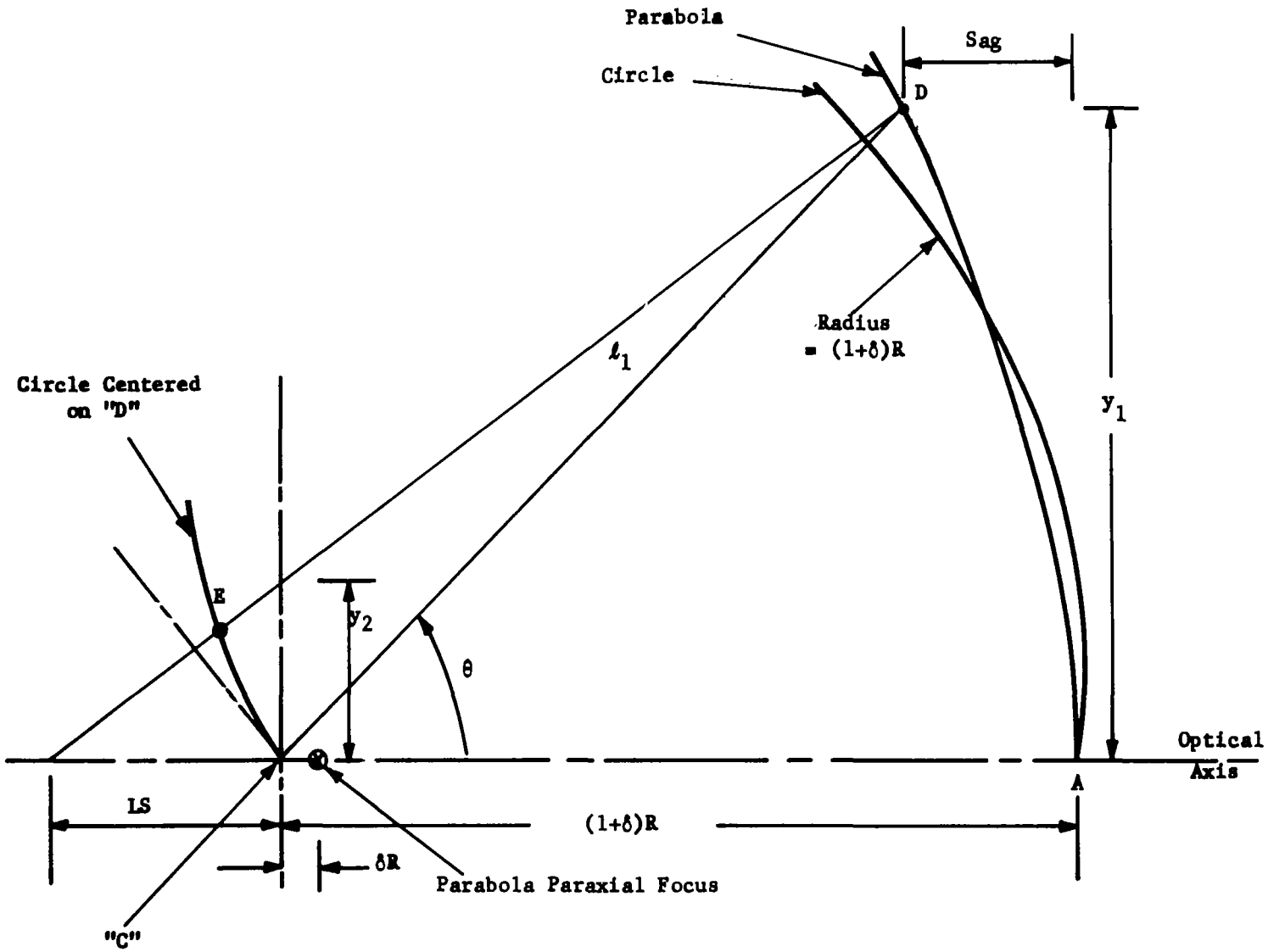

Figure 33. Geometry for Calculating OPD of a Parabola When Viewed from its Nominal Center of Curvature

$$\text{marginal path} = 2\,\ell_1$$

$$\text{paraxial path} = 2(1 + \delta)R$$

$$\text{OPD} = \frac{\text{(marginal path)} - \text{(paraxial path)}}{\lambda}$$

where:

$\delta = \frac{\Delta R}{R}$ = fractional displacement of parabola paraxial focus from point "C", the focus of Lens-1

θ = ray elevation angle

y = distance above the optical axis of the ray intercept with the parabola

R = paraxial radius of curvature of parabola

OPD = optical path difference in units of wavelength

Notice that the insert in the left-hand corner of Figure 6 clarifies the difference between the axial displacement of the parabola from a sphere, Δz, and the optical path length difference, Δ path, between the two for divergent illumination. When $\delta = 0$, the parabola paraxial focus coincides with the focus point of Lens-1.

Values of OPD were calculated as a function of θ for several values of δ and for R = 400 mm. These are plotted in Figure 34 where values of θ have been normalized to:

$$\text{Ray Position} = \frac{\tan\theta}{0.25}$$

The calculator program was then reorganized to solve for ray positions for integral number values of OPD. These positions then represented the normalized positions for constructive interference in the fringe pattern. For ray positions between 0.20 and 0.93, the positions of 200 fringes were computed. These data then formed the basis of a procurement specification for a reference master for testing the f/1 parabola. A copy of this specification is contained in Appendix A.

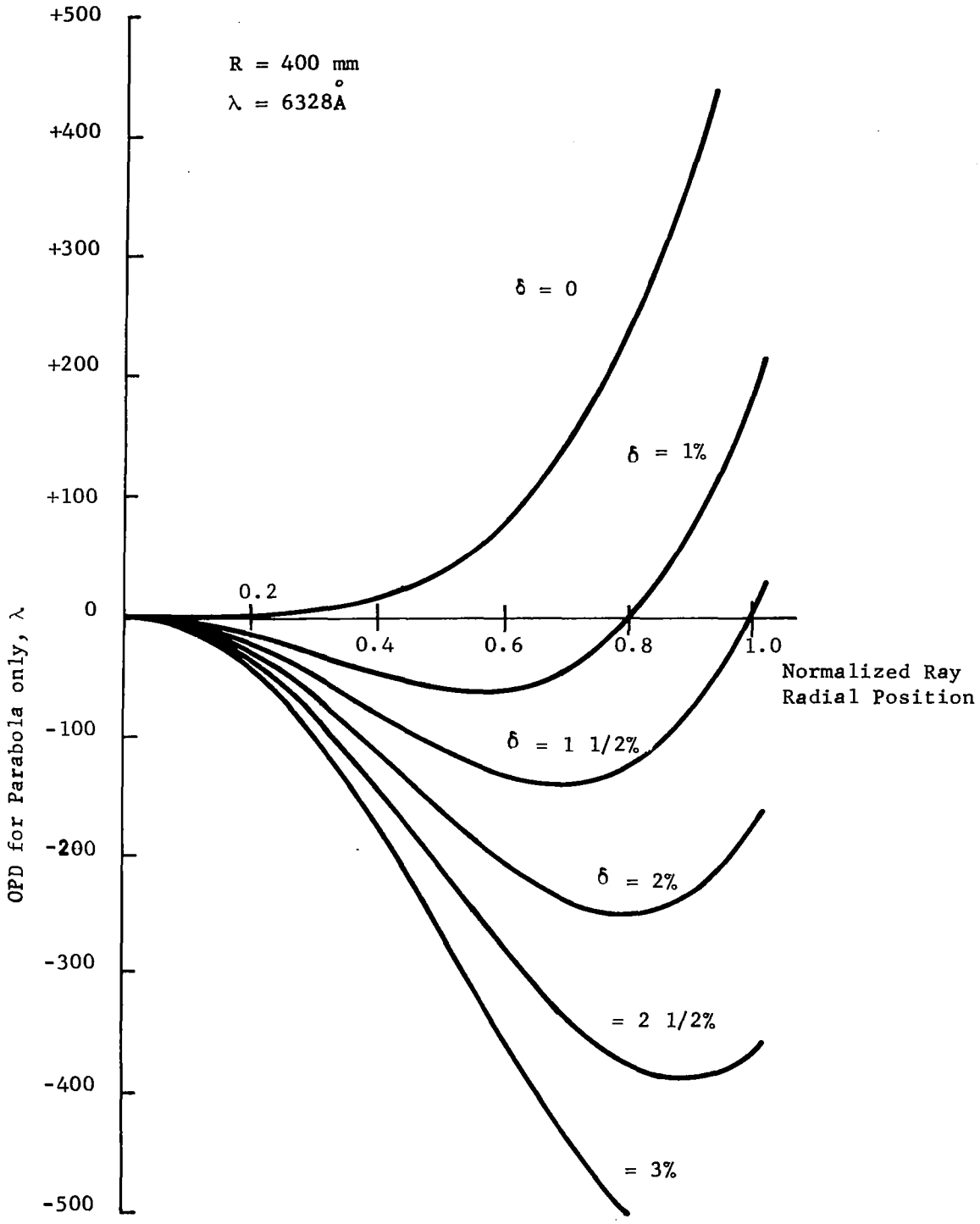

Figure 34. Calculated Optical Path Difference between a Parabola and a Sphere When Viewed from the Nominal Center of Curvature.

A reference pattern was purchased from the Qualitron Corp. of Danbury, Connecticut. Figure 8(a) in the summary is an enlargement from this master. Figure 8(b) is an actual fringe pattern made with an f/1, 8-inch parabola and an f/1 spherical reference reflector in the two interferometer arms. Figures 8(c) and 8(d) show the moiré pattern obtained by multiplying the actual fringe pattern with the calculated pattern. Figure 8(c) was made with optimum alignment of the patterns. It shows approximately four fringes of spherical aberration and one and one half fringe of astigmatism. This is attributed to distortions in the field lens which were not considered in the calculations. Figure 8(d) was made with the reference mirror tilted slightly. A perfect optical system would have produced straight lines. The spherical errors are easier to identify in this figure.

5. SECONDARY ALIGNMENT

A short study was conducted to determine the feasibility of using the primary mirror figure sensor to measure the secondary alignment also. The study results show that conceptually this can be done with sufficient sensitivity; but further investigation is required to determine if the additional optical components can be made with the required precision.

The fundamental primary-to-secondary alignment requirement can be easily visualized if we draw a simple picture of a Gregorian telescope. (See Figure 35.) For a remote on-axis source, the paraboloid primary will form a spherical wavefront converging on its prime focus point. The ellipsoid secondary will, by definition, relay a point source at one focus to its second focal point. Hence the fundamental alignment requirement is that the primary focus coincide with one secondary focus (Ref. 11). It was shown during the Stratoscope II development that other factors are of less consequence than this requirement. This criterion applies equally well to a Cassegrain telescope.

Figure 36 shows the optical arrangement for performing both primary and secondary alignment measurements. An extra element, Lens-2, has been added to make the central portion of the interferometer beam converge at the primary prime focus. Also a spherical surface has been added to the back of the secondary mirror. This surface is made concentric about the prime focus. The figure sensor then measures axial and lateral displacements of the spherical surface center of curvature relative to the prime focus point.

The equations used to establish secondary alignment tolerances are as following (Ref. 12):

$$\delta_a = 8 \left(\frac{\lambda}{n}\right) (f/no)^2 \times k$$

$$\delta_\ell = 64 \left(\frac{\lambda}{n}\right) (f/no)^3$$

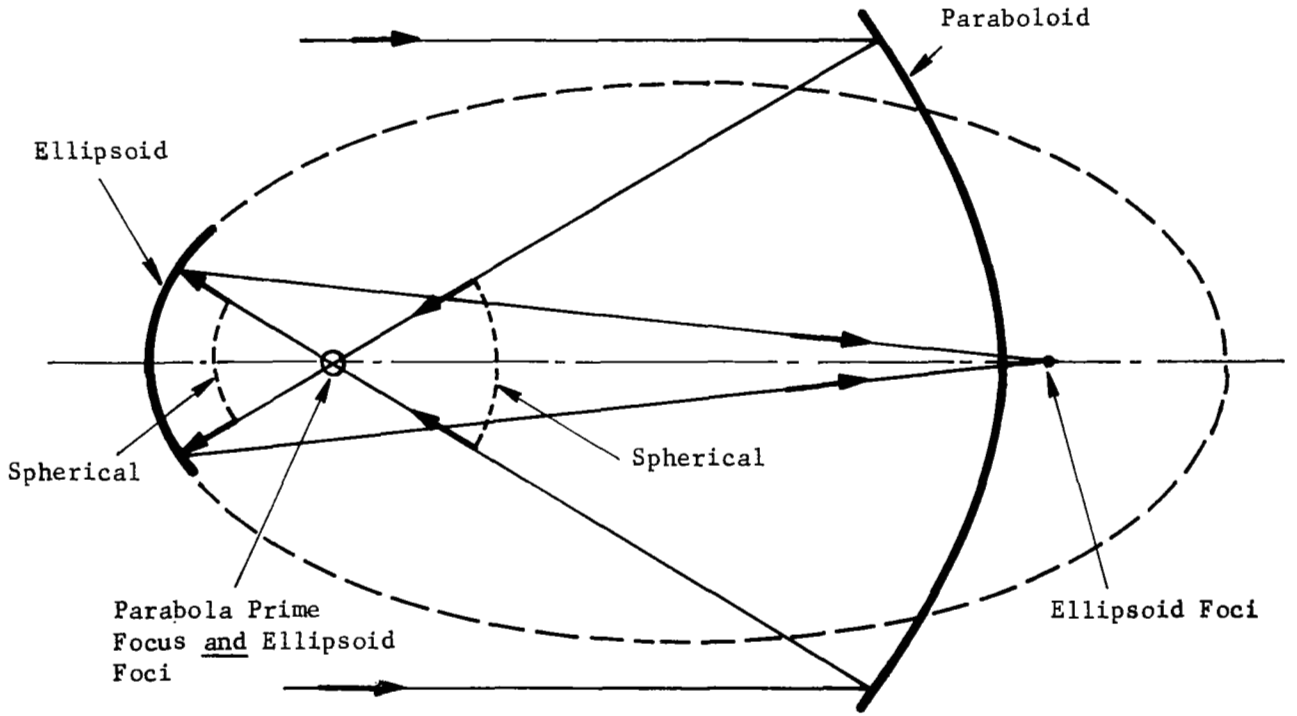

Figure 35. Geometry of Primary-Secondary Alignment Showing Coincidence of Primary Prime Focus and Secondary Foci for a Gregorian Telescope System

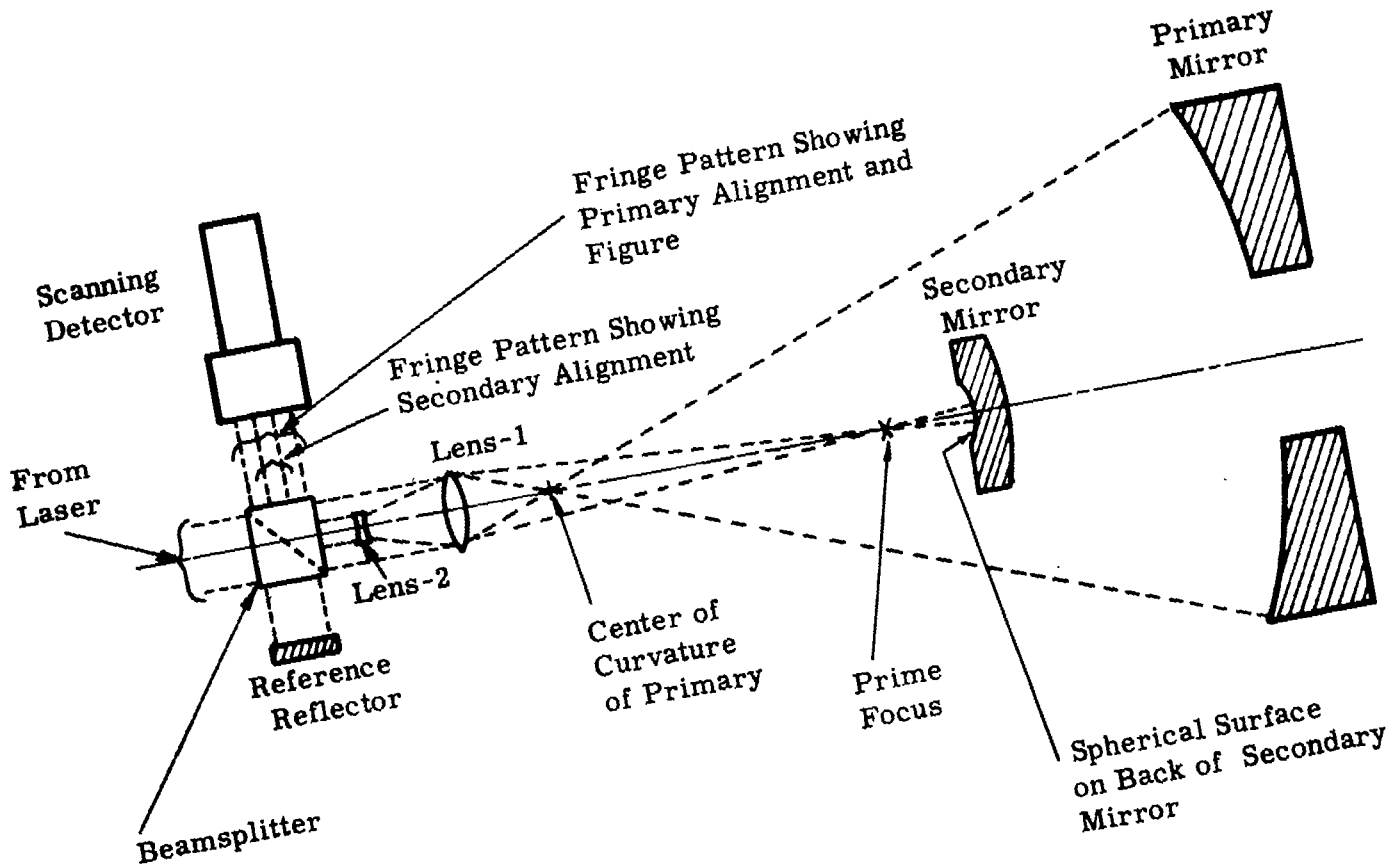

...gement for Measuring Primary - Secondary Alignment with the Primary

where:

δ_a = axial misalignment tolerance

δ_ℓ = lateral misalignment tolerance

λ/n = peak wavefront error permitted

K = constant

A value of n = 10 was used. This results in a Strehl ratio of 97 percent. The factor K accounts for the fact that a major portion of the axial focus error will be compensated for by a focal adjustment at the instrument focal plane. A value of K = 100 was used. The following numerical values were used for the computation of secondary alignment tolerances:

Primary Mirror	f/1.5; f.l. = 150 inches
Secondary Mirror	20% obscuration
Interferometer Beam	3 inch diameter
Lateral Alignment Tolerance	±0.0004 inch
Axial Alignment Tolerance	±0.005 inch

Calculations indicate that a lateral misalignment of 0.0004 inch causes approximately $\lambda/3$ of relative tilt across the test beam of the interferometer. This is easily detected. Axial misalignment of 0.005 inch causes a wavefront change in the interferometer of $\lambda/50$. This is just about at the limit of sensitivity as determined by available signal-to-noise ratio.

The combination of Lens-2 and Lens-1 actually forms a measuring arm which locates a spot at the prime focus relative to the center of curvature of the primary. Small changes in either lens characteristic or location will produce large changes in the position of this spot. For example: The spacing between Lens-1 and Lens-2 must be maintained to ±2 microinches over a distance of approximately 6 inches, and the angular alignment of the lens pair must be correct to within approximately ± 1/2 arc-second. Previous experience indicates that these dimensional tolerances can be met during manufacture for a specific set of environmental conditions. Whether or not they can be maintained in a spaceborne telescope depends upon how much of an environmental variation must be tolerated, especially with regard to the spacing tolerance.

6. INTERFEROMETER

In the course of performing the work described in the previous sections, it was necessary to consider the optimum configuration for the interferometer. Earlier work had been done with a Twyman-Green interferometer having a simple plate beamsplitter. It soon became apparent that a cube beamsplitter would be best to minimize distortion due to the spherical wavefront passing through the beamsplitter. Also, because of its symmetry, the cube to a large extent compensates effects of spherical aberration in the two beam paths. Two different cube beamsplitters were evaluated: one using an Inconel semi-reflecting surface, and a second using a recently developed polarization sensitive semi-reflector.

The Twyman-Green interferometer with Lens-1 in one beam path results in more optical surfaces within the optical interference paths than might be desired for best accuracy. Therefore, the recommended design is a modification that places Lens-1 between the laser and beamsplitter so that only the beamsplitter, reference reflector, and element under test contribute to the interference effects. This arrangement is described in this section.

6.1 Polarization Interferometer

The use of a polarizing beamsplitter was investigated for use in the interferometer. It was found to work well, but is not recommended for this application because of the complexity of the additional optical elements required. Nevertheless the following will describe its use.

The key element of the polarization interferometer is a device called a polarizing beamsplitter, recently invented at Perkin-Elmer. In the polarizing beamsplitter, the metallic Inconel film of conventional beamsplitters is replaced with a multilayer dielectric stack, that is arranged for the light of one polarization to be transmitted, while light of the opposite polarization is reflected. Because the layers are made of dielectric material, the losses are negligible.

Figure 37 shows an interferometer that utilizes a polarizing beamsplitter. The polarization sensitive layer is arranged to transmit light polarized with

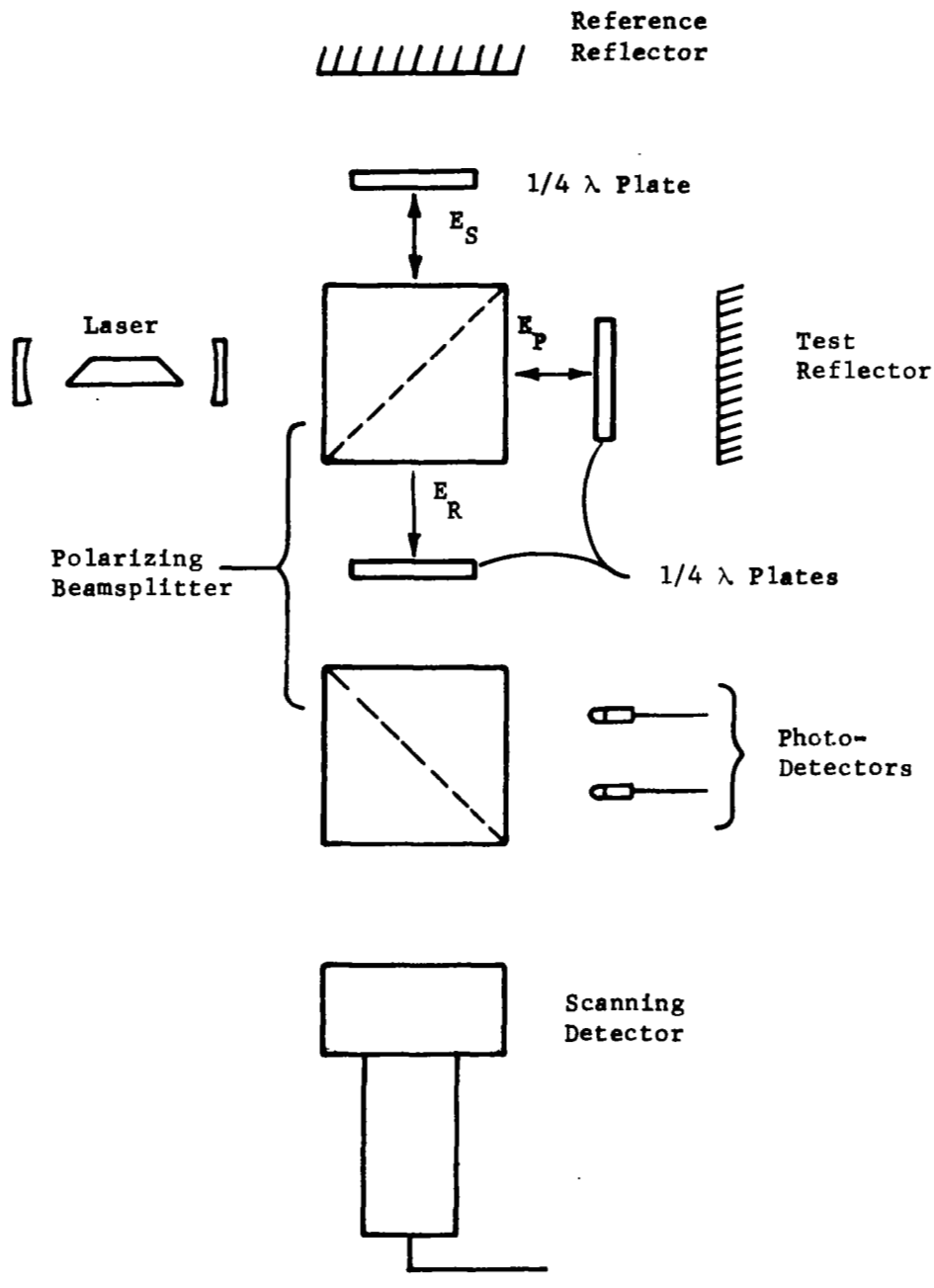

Figure 37. Twyman-Green Interferometer Using A Polarizing Beamsplitter

the E vector parallel to the plane of the paper, E_p, and to reflect light polarized normal to the paper, E_s. The laser is oriented with its polarization plane at 45 degrees so that equal components are transmitted and reflected on the first pass through the beamsplitter. Each arm contains a 1/4 λ plate, which converts the beams into circularly polarized light. Each beam is then reflected by a mirror and passed back through the 1/4 λ plate. The net result is a 90-degree change in the polarization of the light in each arm. This means that all light incident upon the input arm of the beamsplitter emerges from the output arm only.

In the output arm, the two beams are polarized at right angles to each other and no inteference takes place. However, interference fringes can be generated by placing a 1/4 λ plate and a polarization analyzer in the output arm. The reason for this may be visualized by referring to Figure 38. The 1/4 λ plate in the output is oriented so that it changes each output beam into circularly polarized light, one left-hand and one right-hand. The figure illustrates that the vector addition of two counterrotating vectors of equal amplitude produces a resultant vector, E_R, which changes in amplitude but is fixed in polarization. The orientation of E_R is determined by the relative phase of the two rotating vectors. Referring again to Figure 37, note that a change in the length of either interferometer arm changes the phase between the two output vectors, resulting in angular rotation of the plane or polarization of the resultant vector E_R by an angle equal to half the phase angle change. Transmitting the resultant vector through a polarization analyzer will produce an intensity related to the relative orientation of E_R and the analyzer. The resulting interference pattern is equivalent to the intensity pattern obtained with an interferometer using a conventional beamsplitter.

The polarizing interferometer is no more efficient than the ideal interferometer with a lossless beamsplitter, since half of the light is absorbed in the polarization analyzer. However, by using a second polarizing beamsplitter in place of the analyzer, it is possible to have two sets of detectors with the result that over 95 percent of the laser output may be used as compared to only 50 percent for the conventional interferometer with a dielectric beamsplitter.

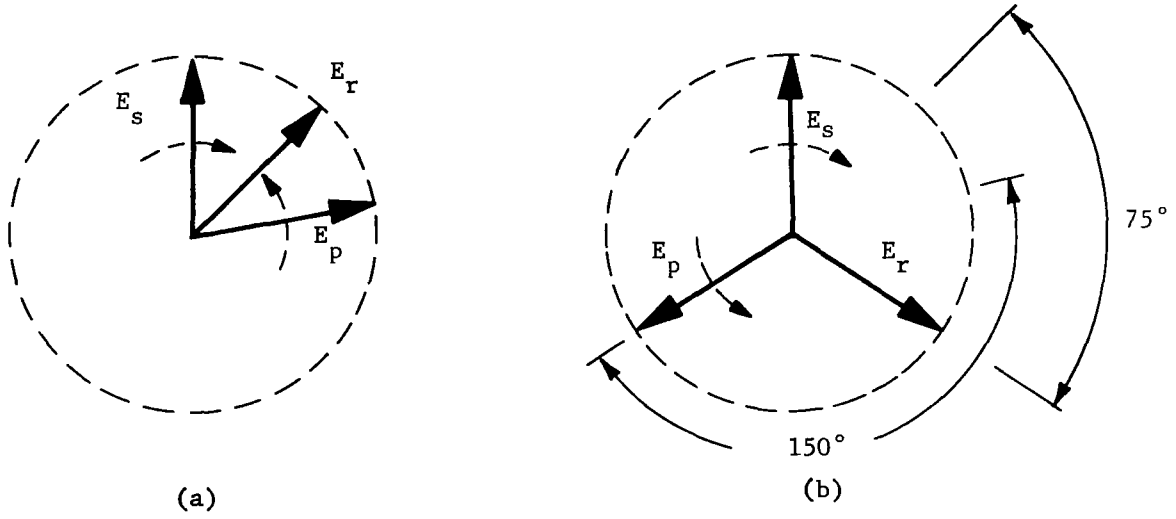

Figure 38. Vector Representation of the Summation of Right-hand and Left-hand Circularly Polarized Light for Two Different Relative Phases Between The Two Inputs

6.2 Optical Arrangement

The Twyman-Green interferometer requires that Lens-1 be in one of the beams. This results in six extra surfaces, each traversed twice, within the interference path. It would be desirable to eliminate these. Lens-1 also contributes additional spherical aberration which must be included in the moiré reference master. It was therefore decided to move Lens-1 to the interferometer input arm.

Figure 39 shows the recommended optical arrangement for the interferometer. Drawings for the key optical components in this assembly are contained in Appendix B. Figure 40 shows the recommended overall block diagram for a "working model" of the Advanced Figure Sensor.

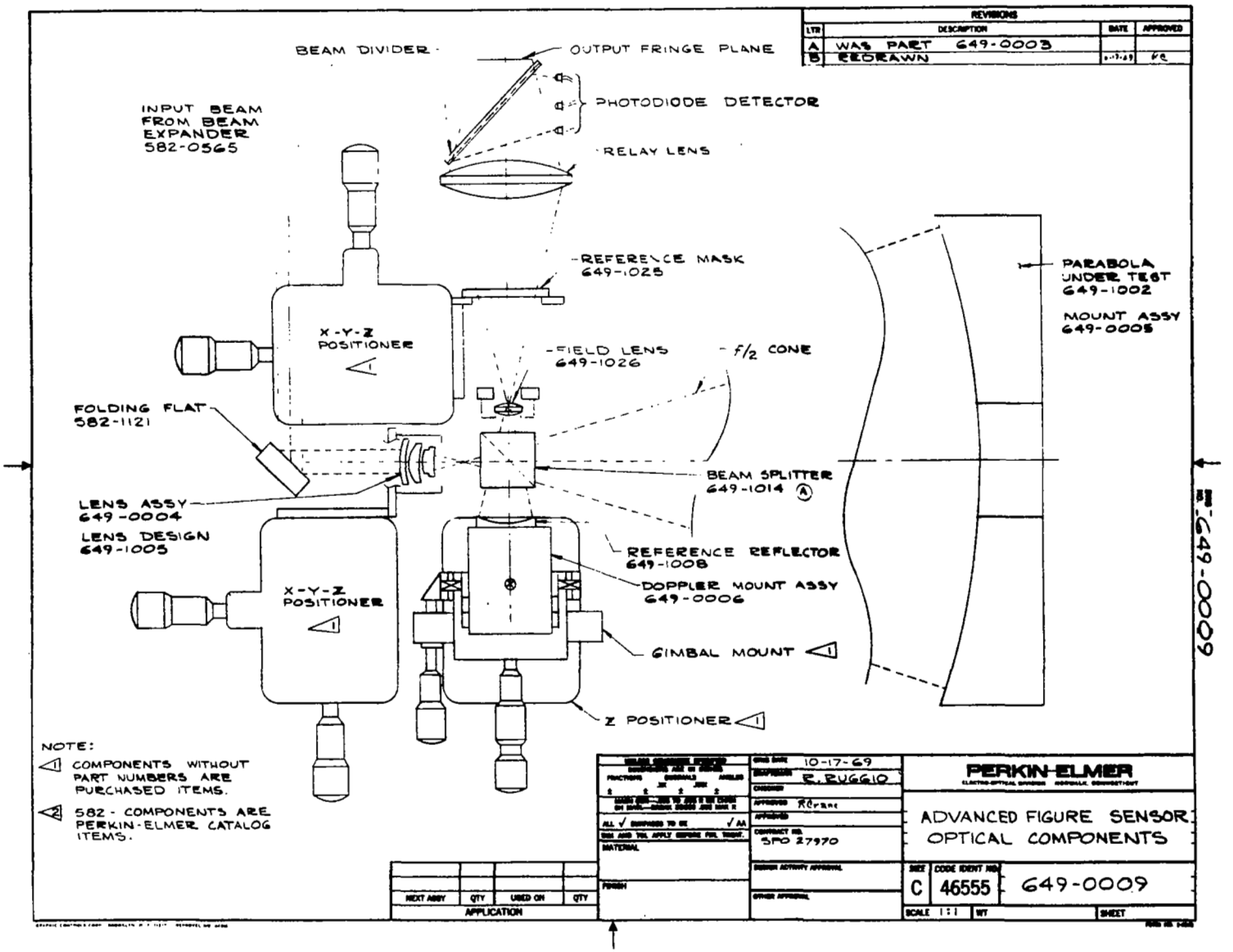

Figure 39. Advanced Figure Sensor Optical Components

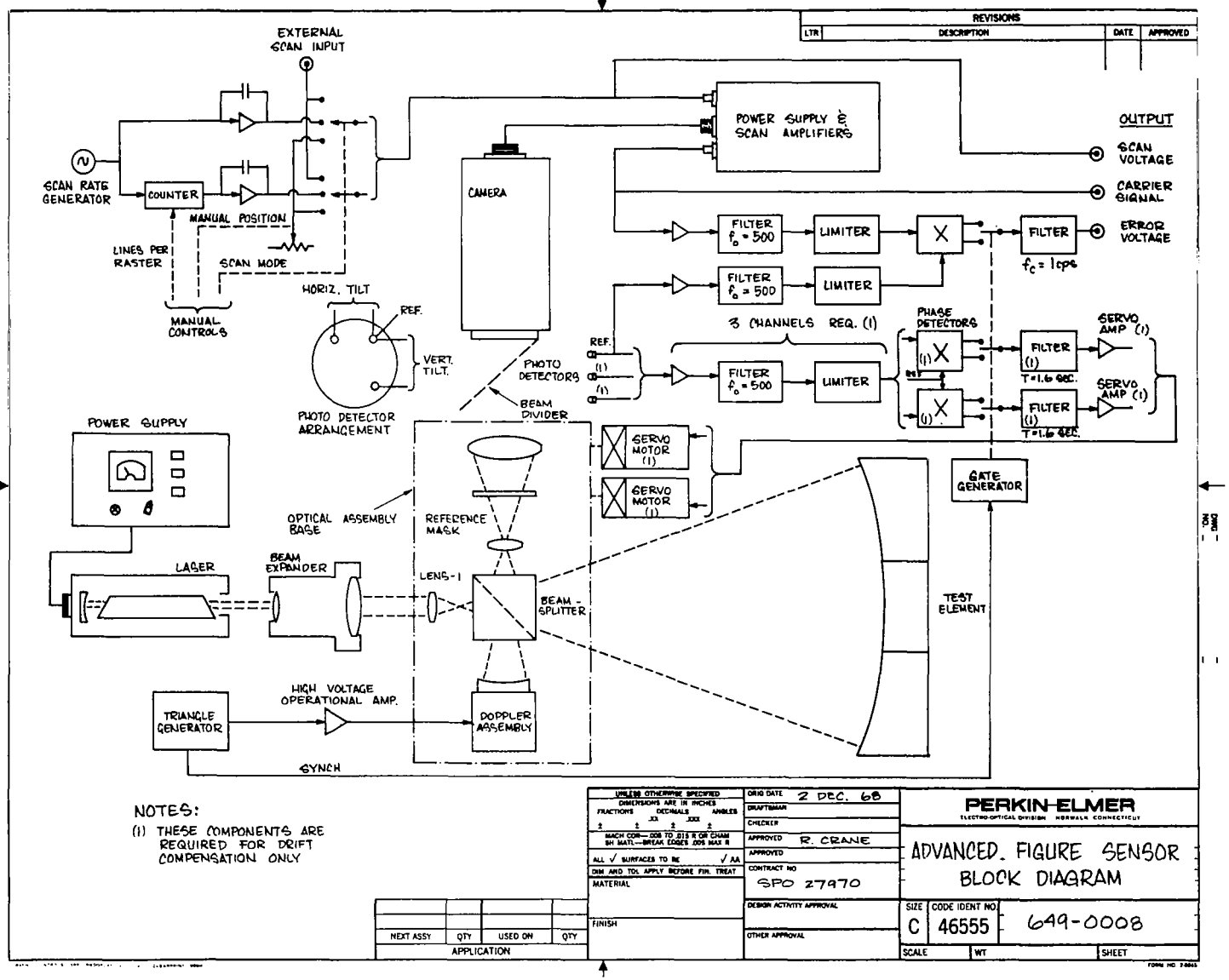

Figure 40. Advanced Figure Sensor Block Diagram

REFERENCES

1. Robertson, H.J.: Active Optical System for Spaceborne Telescopes. NASA CR-66297, The Perkin-Elmer Corporation, Oct. 1966.

2. Robertson, H.J.: Active Optical System for Spaceborne Telescopes Final Report. NASA CR-66489, The Perkin-Elmer Corporation, Dec. 1967.

3. New Developments in Interferometry. The Perkin-Elmer Corporation, Sept. 1967.

4. Staff of the Perkin-Elmer Corporation: Advanced Optical Figure Sensor Techniques. Report No. 8660, The Perkin-Elmer Corporation, Jan. 1968.

5. Crane, R.: Interference Phase Measurement. Applied Optics, vol. 8, no. 3, Mar. 1969, p. 538.

6. Crane, R.: An Experimental 20-Inch Segmented Active Mirror. IEEE Trans. AES, March 1969.

7. Frocht, M.M.: Photoelasticity. John Wiley & Sons, 1948, p. 137.

8. Offner, A.: A Null Corrector for Paraboloidal Mirrors. Applied Optics, vol. 2, no. 2, Feb. 1963, pp. 153-155.

9. Langenbeck, P.: Optical Wavefront Mapping by Dual Interferometry, J. Opt. Soc. Amer., vol. 58, no. 4, Apr. 1968, p. 499.

10. Roark, R.J.: Formulas for Stress and Strain. McGraw-Hill Book Co.,Inc., 1965.

11. Smith, W.: Modern Optical Engineering. McGraw-Hill Book Co., Inc.,1966, pp. 389-390.

12. Staff of the Perkin-Elmer Corporation: Princeton Advanced Satellite Study, Final Report. Report No. 8346(III) (Subcontract No. 1 to NASA Grant NGR-31-001-044), The Perkin-Elmer Corporation, 1966, pp. B47-B53.

APPENDIX A

REFERENCE MASTER

CODE IDENT. 46555	PERKIN-ELMER ELECTRO-OPTICAL DIVISION, NORWALK, CONN.	DATE: 12/10/68

SPECIFICATION

REFERENCE MASTER

1.0 Pattern Description

200 Concentric circles or rings, alternately opaque and transparent, where the dark ring radii are defined by an equation of the form

$$a\,r^2 + b\,r^4 + C\,r^6 = n$$

Where: n = ring number
r = ring radius
a, b and c are constants

See figure 1 for approximate pattern

2.0 Pattern Data

2.1 Circle Radii: See Table I for relative values of circle radii and thickness normalized to an outer circle radius of exactly 1.0

2.2 Pattern Size: Absolute radius of outercircle (ring number 200)

3.0 Accuracy

3.1 Resolution:	response	95% at 50 lines/mm
	response	75% at 80 lines/mm
3.2 Circle Radii		± 0.00005 inch
3.3 Circle Concentricity:		± 0.00005 inch
3.4 Circle Thickness:		± 5%
3.5 Pattern Scale:		Outer circle radius = ± 0.002 inches

4.0 Substrate

4.1 Material:	glass or equivalent
4.2 Size:	2 x 2 inch^2
4.3 Thickness:	0.060 inch
4.4 Flatness:	± 0.001 inch

CRANE PREPARED BY	R C Crane APPROVED	APPROVED	APPROVED	PE SPEC 649-1025	REV A	SHEET

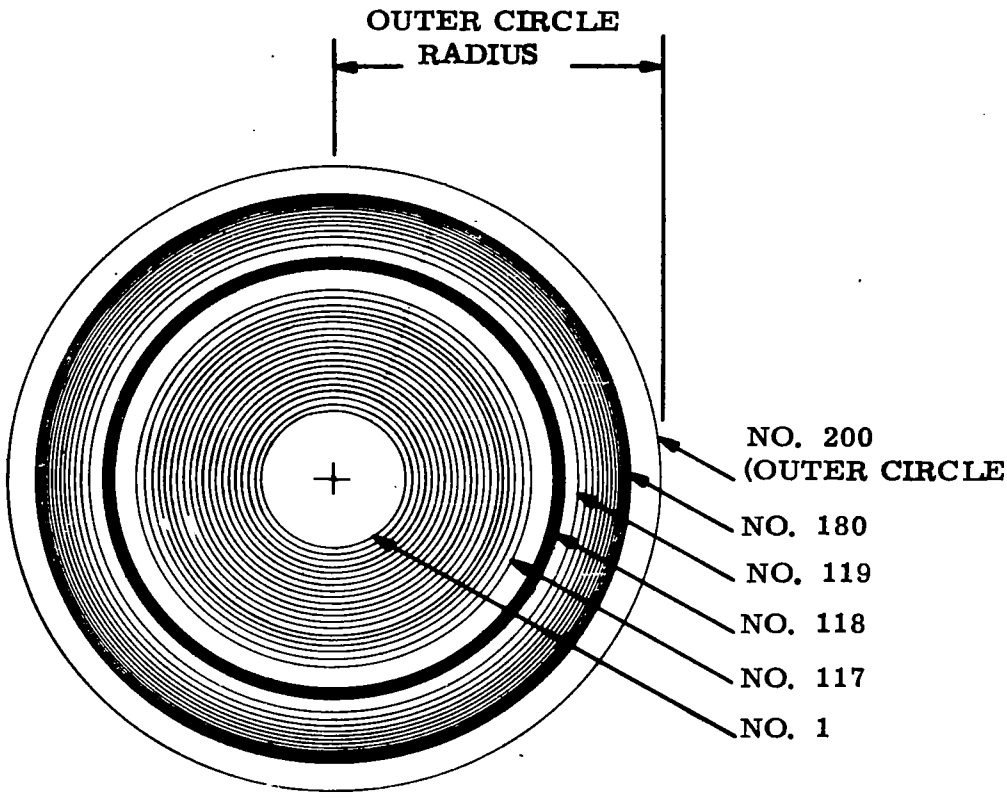

Approximately every fifth ring shown

Figure A-1. Reference Master

APPENDIX B

COPIES OF DRAWINGS

Copies of Drawings

Assemblies

649	0004	f/2 objective assembly
	0005	Parabola mount
	0006	Doppler mount

Details

649	1002	f/1 Parabola
	1005	Lens - 1 Design
	1008	Spherical Reflector
	1014	Beamsplitter

REVISIONS			
LTR	DESCRIPTION	DATE	APPROVED

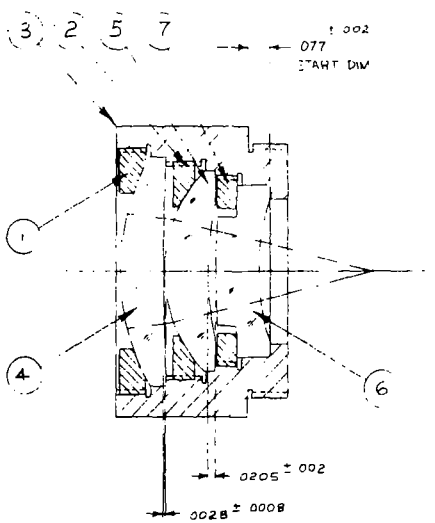

NOTE:-
O.D.D.S. DWG N° 649-1005

QTY REQD	ITEM NO	PART NUMBER	DESCRIPTION	MAT'L/SPEC	CODE IDENT
1	7	649-1013	RETAINER ELEMENT 3		
1	6	649-1012	LENS ELEMENT 3		
1	5	649-1011	LENS ELEMENT 2		
1	4	649-1010	LENS ELEMENT 1		
1	3	649-1009	HOUSING LENS		
1	2	649-1007	RETAINER ELEMENT 2		
1	1	649-1006	RETAINER ELEMENT 1		

LIST OF MATERIALS

APPLICATION			
FINAL	1		
NEXT ASSY	QTY	USED ON	QTY

UNLESS OTHERWISE SPECIFIED DIMENSIONS ARE IN INCHES. FRACTIONS ± .XX, DECIMALS .XX ± .XXX, ANGLES ±
MACH FOR BREAK EDGES AND MAT R
ALL ✓ SURFACES TO BE ✓ AA
DIM AND TOL APPLY BEFORE FIN. TREAT.
MATERIAL: SEE ABOVE
FINISH:

DRG DATE: 20 SEPT 68
DRAFTSMAN: CAH
CHECKER: G. Wasserbeck 9-27-68
APPROVED: J. Cole 9/30/68
APPROVED:
CONTRACT NO.: 27970
DESIGN ACTIVITY APPROVAL:
OTHER APPROVAL:

PERKIN-ELMER
ELECTRO-OPTICAL DIVISION NORWALK, CONNECTICUT

ADVANCED SYSTEMS SENSOR ASSY

SIZE	CODE IDENT NO.	
C	46555	649-0004

SCALE 4:1 | WT | SHEET 1 OF 1

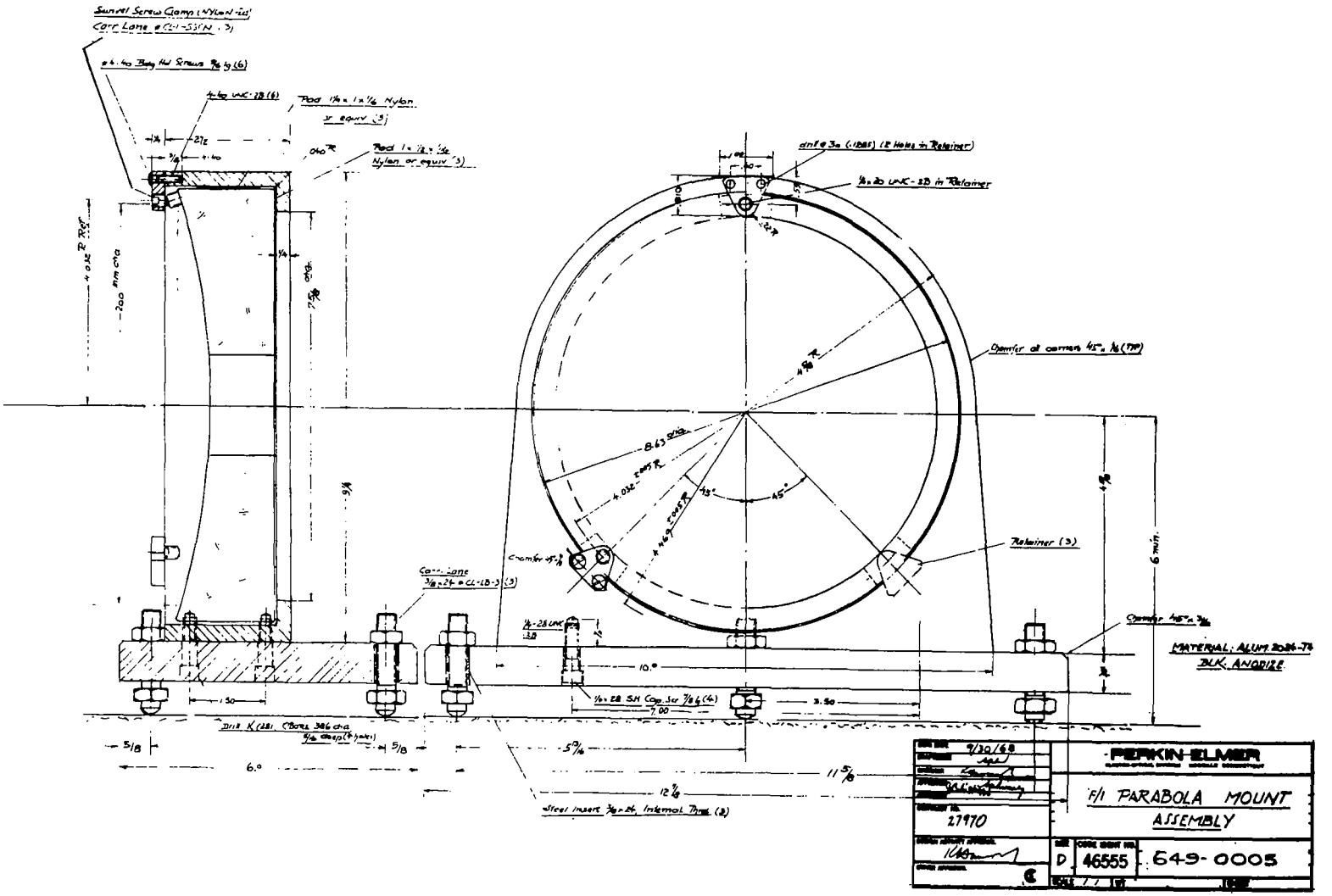
Sunrel Screw Clamp (NYLON-12)
Carr Lane #CL-11-SS(N-3)
#6-40 Binding Hd Screws 3/8 lg (6)
4-40 UNC-2B (6)
Pad 1/8 x 1 x 1/16 Nylon or equiv (3)
Pad 1 x 1/2 x 1/16 Nylon or equiv (3)
.040 R
2 1/2
1/4
7 5/8 dia.
9 1/4
Drill K (281) Clears 386 dia. 3/8 deep (5 holes)
5/8
6.0
5 3/8
11 5/8
12 3/8
Steel Insert 3/8-24, Internal Thrd (2)
Carr Lane 3/8-24 x CL-15-3 (3)
1/4-28 UNC-2B
10.°
3.50
7.00
1/8-28 SH Cap Scr 7/8 lg (4)
Chamfer 45° x 1/8
Retainer (3)
Chamfer at corners 45° x 1/8 (TYP)
4.032 Conv R
4.469 Conv R
.863 Conv R
19°
45°
6 min.
MATERIAL: ALUM 2024-T4
BLK. ANODIZE
PERKIN-ELMER
F/1 PARABOLA MOUNT
ASSEMBLY
27970
D
46555
649-0005

REVISIONS			
LTR	DESCRIPTION	DATE	APPROVED
A	REDRAWN	10-17-69	RC

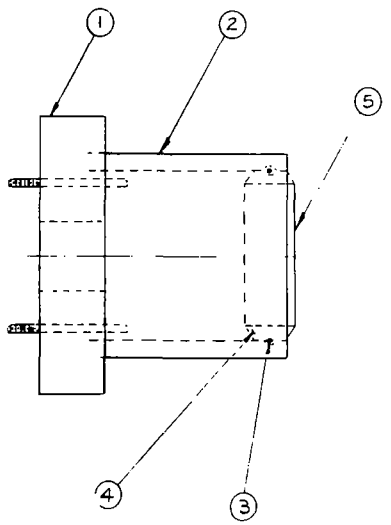

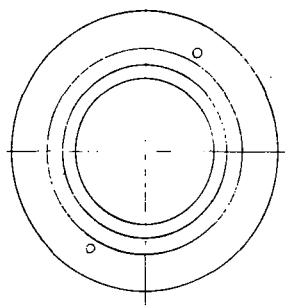

QTY REQD	ITEM NO	PART NUMBER	DESCRIPTION	MATL/SPEC	CODE IDENT
1	5	649-008	MIRROR		
1	4	649-1017	SPACER		
1	3	649-1018	RETAINER SPRING		
1	2	649-015	ACTUATOR		
1	1	649-016	MOUNT PLATE		

LIST OF MATERIALS

NEXT ASSY	QTY	USED ON	QTY

APPLICATION

UNLESS OTHERWISE SPECIFIED DIMENSIONS ARE IN INCHES
FRACTIONS ± — DECIMALS .XX ± — .XXX ± — ANGLES ± —
ALL √ SURFACES TO BE √ AA
MATERIAL —
FINISH —

DRG DATE 0-7-69
DRAFTSMAN R. RUGGIO
CHECKER
APPROVED
APPROVED
CONTRACT NO. SPO 2X970
DESIGN ACTIVITY APPROVAL
OTHER APPROVAL

PERKIN-ELMER
ELECTRO OPTICAL DIVISION NORWALK CONNECTICUT

DOPPLER MOUNT

SIZE	CODE IDENT NO.	DWG NO.
C	46555	649-0006

SCALE — WT SHEET

649-0006

DWG NO. 649-1002

	RADIUS	CC	CX	TOL.	SURFACE CODE	FIGURE TOL P-V	COATING TYPE	COATING CODE	COATING SPEC	COATING λ	CEMENTING	CLEAR APERTURE
R_1	400 <1>	X	-	±10.0	80/50	1/20λ	Al+SiO			6328	TO R OF	<2>
R_2	PLANO	-	-	—	GRIND	— λ	NONE				TO R OF	—
R_3						λ					TO R OF	
R_4						λ					TO R OF	

UNLESS OTHERWISE SPECIFIED
MINIMUM PROTECTIVE BEVEL ON ALL CORNERS AND EDGES
MELT VARIATIONS (DO) (DO NOT) REQUIRE RECOMPUTATION

RECOMPUTATION FOR SPECIFIC MELT DATA

SPO/WO	MELT DATA SHEET	MELT NO.	ND	V	AXIAL THICK. & TOL.	R_1	CC	CX	TOL.	R_2	CC	CX	TOL.

REVISIONS			
LTR	DESCRIPTION	DATE	APPROVED
B	REDRAWN	10-17-69	RC

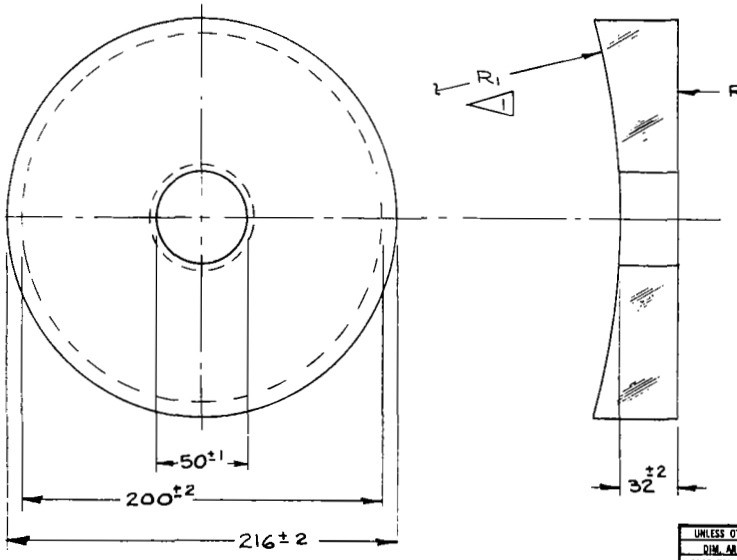

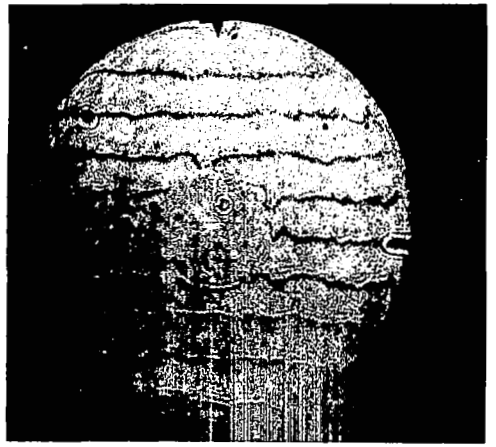

<2> FIGURE TOLERANCE TO BE MAINTAINED WITHIN CENTRAL 200 MM DIAMETER EXCEPT WITHIN 4 MM OF HOLE.

<1> R_1 TO BE FIGURED TO A PARABOLA SURFACE

				649-0001	1
MILLIMETER	INCH	NEXT ASSY	QTY	USED ON	QTY
CONVERSIONS		APPLICATION			

UNLESS OTHERWISE SPECIFIED DIM. ARE IN MILLIMETERS
WEDGE TOL — (MIN.) (SEC.)
PYRAMID TOL — (MIN.) (SEC.)
MATERIAL: SOLID ULE FUSED SILICA

ORIG. DATE 10-17-69
DR R. RUGGIO
CHKR
APPD R Crane
APPD
CONTRACT NO. SPO 27970
DESIGN ACTIVITY APPROVAL
OTHER APPROVAL

PERKIN-ELMER
ELECTRO-OPTICAL DIVISION NORWALK, CONNECTICUT

f/1 PARABOLA

SIZE B | CODE IDENT NO. 46555 | 649-1002
SCALE — | WT | SHEET

FORM NO. 2-0250

DILVIE PRESS INC BROOKLYN 17, N Y REPROVEL NO 440M

SO/WO NO.	REVISIONS			
27970	LTR.	DESCRIPTION	DATE	APPROVED
SERIAL NO.	A	RETYPED	10/17/69	
SETS OF GLASS:				

SURF.	RADIUS	THICKNESS	GLASS	AIR	SURFACE CODE	FIGURE TOL. λ *	CLEAR APERT.	GLASS TYPE	MELT NUMBER
1	19.87 ± .02	4.0 ± .1	✓		60-40	1/20λ	10.0	SF15	✓ **
2	415.14 ± .4	.07 ± .02		✓	60-40	1/20λ	9.3		
3	12.31 ± .01	4.0 ± .1	✓		60-40	1/20λ	9.0	SF15	✓
4	21.00 ± .02	.52 ± .05		✓	60-40	1/20λ	7.2		
5	69.537 ± .05	4.0 ± .1	✓		60-40	1/20λ	7.0	SF15	✓
6	19.87 ± .02	10.43		✓	60-40	1/20λ	5.3		

REMARKS: EFL = 20.00
BFL = 10.43
RMS OPD = .017λ @ 6328Å

*The figure tolerance is based on optimum performance without aspherizing; it may be relaxed and the system corrected at surface #1.

**The lens will perform if index variation is less than ±.001 from catalogue and all of one melt.

DRAWING NO.

DATE	CONTRACT NO.
15 August 68	
OPTICAL DESIGNER	USED ON
F.W. Foster	
CHECKER / DATE	UNLESS OTHERWISE SPECIFIED DIMENSIONS ARE IN MILLIMETERS
APP'VD. BY (OPT. DESIGN) / DATE	MELT VARIATIONS
APP'VD. BY (PROJ. ENG.) / DATE	☐ DO ☐ DO NOT REQUIRE RECOMPUTATION
APP'VD. BY (MECH. DES.) / DATE	\ INDICATES CATALOGUE VALUE ONLY

PERKIN-ELMER
ELECTRO-OPTICAL DIVISION — NORWALK, CONNECTICUT

OPTICAL DESIGN DATA SHEET

☑ CATALOG DESIGN ☐ MELT RECOMPUTATION

SIZE	CODE IDENT. NO.	
A	46555	f/2 OBJECTIVE

SHEET

DWG NO 649-1008

	RADIUS	CC	CX	TOL.	SURFACE CODE	FIGURE TOL P−	COATING TYPE	COATING CODE	COATING SPEC	COATING λ	CEMENTING	CLEAR APERTURE
R_1	1.50	X	−	±.07	80/50	1/20 λ	Al + SiO		1	6328	TO R OF	0.75
R_2	PLANO	−	−	−	GRIND	− λ	NONE				TO R OF	
R_3						λ					TO R OF	
R_4						λ					TO R OF	

UNLESS OTHERWISE SPECIFIED
MINIMUM PROTECTIVE BEVEL ON ALL CORNERS AND EDGES
MELT VARIATIONS (DO) (DO NOT) REQUIRE RECOMPUTATION

REVISIONS

LTR	DESCRIPTION	DATE	APPROVED
A	REDRAWN	10-17-69	RC

RECOMPUTATION FOR SPECIFIC MELT DATA

SPO/WO	MELT DATA SHEET	MELT NO	No	V	AXIAL THICK & TOL	R_1	CC	CX	TOL.	R_2	CC	CX	TOL.

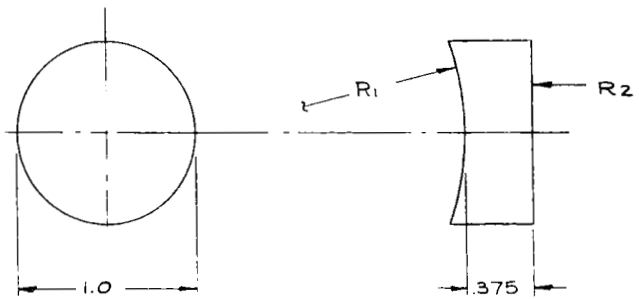

1 EDGES MAY BE BEVELED.

MILLIMETER	INCH	NEXT ASSY	QTY	USED ON	QTY
CONVERSIONS		APPLICATION			

UNLESS OTHERWISE SPECIFIED
DIM. ARE IN INCHES
WEDGE TOL (MIN.) (SEC.)
PYRAMID TOL (MIN.) (SEC.)
MATERIAL: HIGH QUALITY FUSED SILICA

ORIG DATE 10-17-69
DR R. RUGGIO
CHKR
APPD R Crane
APPD
CONTRACT NO SPO 27970
DESIGN ACTIVITY APPROVAL
OTHER APPROVAL

PERKIN-ELMER
ELECTRO OPTICAL DIVISION NORWALK CONNECTICUT

SPHERICAL MIRROR

SIZE B | CODE IDENT NO 46555 | 649-1008
SCALE 2/1 | WT — | SHEET —

FORM NO 30750

80

DWG NO. 649-1014

RADIUS	CC	CX	TOL.	SURFACE CODE	FIGURE TOL.	COATING TYPE	COATING CODE	COATING SPEC	COATING λ	CEMENTING	CLEAR APERTURE
R_1 R_5 ∞			3/8	80-50	1/20 λ	VLR			.63	TO R OF	22
R_2 R_6 ∞			3/8	80-50	1/20 λ	VLR			.63	TO R OF	22
R_3 ∞			3/20	80-50	1/20 λ	NOTE 1				TO R OF	29
R_4 ∞			3/20	80-50	1/20 λ	NONE				TO R OF	29

RECOMPUTATION FOR SPECIFIC MELT DATA

SPO/WO	MELT DATA SHEET	MELT NO.	ND	V	AXIAL THICK. & TOL.	R_1	CC	CX	TOL.	R_2	CC	CX	TOL.

UNLESS OTHERWISE SPECIFIED
MINIMUM PROTECTIVE BEVEL ON ALL CORNERS AND EDGES
MELT VARIATIONS (DO) (DO NOT) REQUIRE RECOMPUTATION

REVISIONS			
LTR	DESCRIPTION	DATE	APPROVED
A	REDRAWN	10-17-67	RC

NOTE 2

NOTE 3

ASSEMBLY

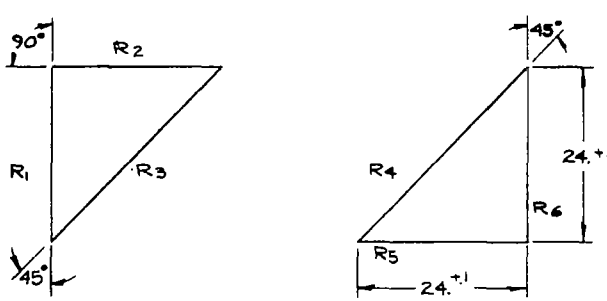

ELEMENT 1 ELEMENT 2

4. ALL ANGLES ±5 MIN
3. NON-OPTICAL SURFACES TO BE CLOTH POLISHED
2. WEDGE AND SCATTER OF R_3-R_4 TO BE SMALLEST READILY AVAILABLE. USE WEST COAST CEMENT.
1. INCONEL BEAMSPLITTER COATING. INTENSITY TRANSMITTED ≈ .5 % INTENSITY REFLECTED.

CONVERSIONS		APPLICATION			
MILLIMETER	INCH	NEXT ASSY	QTY	USED ON	QTY

UNLESS OTHERWISE SPECIFIED DIM. ARE IN MILLIMETERS
WEDGE TOL. 0.001 (SEC.)
PYRAMID TOL. 0.001 (SEC.)
MATERIAL: BK-7 Δn = 2×10⁻⁶ CLASS A STRIAE

ORIG DATE 10-17-67
DR R. RUGGIO
CHKR
APPD R Crane
APPD
CONTRACT NO. 27970
DESIGN ACTIVITY APPROVAL
OTHER APPROVAL

PERKIN-ELMER
ELECTRO-OPTICAL DIVISION NORWALK, CONNECTICUT

INCONEL BEAMSPLITTER

SIZE	CODE IDENT NO.	649-1014
B	46555	

SCALE WT SHEET